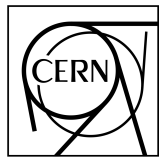


EUROPEAN ORGANIZATION FOR NUCLEAR RESEARCH



ALICE-ANA-2014-xxx
May 26, 2015

Λ to K_S^0 ratio inside and outside Jets in p–Pb collisions at $\sqrt{s_{NN}} = 5.02$ TeV with ALICE

Xiaoming Zhang¹, Jana Bielčíková², Vít Kučera^{2,3}, Mateusz Płoskoń¹

1. RNC, Lawrence Berkeley National Laboratory, Berkeley
2, Acad. of Sciences of the Czech Rep., Prague
3, IPHC, Strasbourg

Email: xzhang@cern.ch

Abstract

It has been found that the baryon to meson ratio at intermediate transverse momentum (p_T) is up to a factor two larger in the systems such as Pb–Pb but also p–Pb collisions than that in proton–proton collisions. Particle production at intermediate p_T is expected to have contributions from hadronization of the medium as well as from fragmentation of high-momentum partons. To disentangle the different contributions, ALICE is studying particle production in reconstructed jets and the underlying event separately.

In this contribution, we present the p_T distributions of reconstructed K_S^0 and Λ associated with a jet and with the underlying event in p–Pb collisions at the LHC. The hard scatterings are selected on an event-by-event basis by anti- k_T jets with resolution parameter $R = 0.4$ (or $R = 0.2$) reconstructed from charged particles with a minimum p_T of 10 (or 20) GeV/c. We will discuss the resulting baryon-to-meson ratio inside and outside jets together with the inclusive measurements in several event multiplicity bins of p–Pb collisions.

Contents

1	Introduction	3
2	Data Sample	3
2.1	Data	3
2.2	MC	4
2.2.1	DPMjet simulations	4
2.2.2	PYTHIA simulations	4
3	Inclusive V⁰s Analysis: Comparison the PWG-LF Results	5
3.1	Event selection of inclusive V ⁰ analysis	5
3.2	V ⁰ candidate selection	6
3.3	Analysis strategy	7
3.4	Comparison to the LF results	9
4	Charged Jets Analysis	13
4.1	Inclusive jets reconstruction	13
4.2	Jet background density	14
4.3	Background fluctuations	17
4.4	Detector response matrix	17
5	Production of V⁰s in Jets	18
5.1	Analysis strategy	18
5.1.1	Acceptance	18
5.1.2	V ⁰ –jet matching	19
5.1.3	Underlying V ⁰ estimation	21
5.2	Efficiency	21
5.2.1	V ⁰ efficiency in MC	21
5.2.2	η modified V ⁰ efficiency	23
5.3	Underlying background subtraction	25
5.4	Feeddown subtraction	27
5.5	Normalized results	28
6	Uncertainty	29
6.1	Statistic uncertainty	29

6.2 Systematic uncertainty	31
6.2.1 Uncertainty on single V^0 analysis	32
6.2.2 Uncertainty on underlying V^0 subtraction	35
6.2.3 Uncertainty on feeddown subtraction	37
6.2.4 Uncertainty on jet p_T	39
7 Results	41
A V^0 Efficiency Calculation with the Weighting Approach	45
B Binomial Errors	48

1 Introduction

This analysis is aimed to shed light on the enhanced baryon to meson ratio in p–A collisions as compared to pp collisions. The p_T differential production yields of Λ baryons and K_S^0 mesons are measured separately in the region of hard scattering tagged with charged particle jet and in the region dominated by the soft particle production: the underlying event (not tagged by the hard scattering).

The Λ and K_S^0 are reconstructed via invariant mass analysis. The jets are reconstructed with the so called hybrid track selection with anti- k_T jet finder with $R = 0.2, 0.3$ and 0.4 . The studies are performed as a function of event activity (event class) according to V0M and ZNA. In each case we find that the peak observed in the inclusive Λ -to- K_S^0 ratio is characteristic to the particles originating from the underlying event, whereas the Λ -to- K_S^0 ratio associated to the charged particle jets (with $p_T > 10$ and $20 \text{ GeV}/c$) is consistent with Pythia simulation of hard scatterings in p-p collisions.

Documents:

- presentation of preview: <https://indico.cern.ch/event/311402/session/11/contribution/67/material/slides/0.pdf>.

2 Data Sample

- p–Pb collisions at $\sqrt{s_{\text{NN}}} = 5.02 \text{ TeV}$.

2.1 Data

- LHC13b pass 3 AOD, 12 runs: 195344, 195346, 195351, 195389, 195390, 195391, 195478, 195479, 195480, 195481, 195482 and 195483;
- LHC13c pass2 AOD, 15 runs: 195529, 195531, 195532, 195566, 195567, 195568, 195592, 195593, 195596, 195633, 195635, 195644, 195673, 195675 and 195677.

Analysis based on the EMCal jet (JE) framework:

- track filter:

```
$ALICE_ROOT/PWG/EMCAL/ AliEmcalPicoTrackMaker.h (.cxx)
```

- jet finder:

```
$ALICE_ROOT/PWGJE/EMCALJetTasks/ AliEmcalJetTask.h (.cxx)
```

- user analysis task derived from:

```
$ALICE_ROOT/PWGJE/EMCALJetTasks/ AliAnalysisTaskEmcalJet.h (.cxx)
```

Events are selected with:

- event trigger: kINT7;

- skip first event chunk:

```
Bool_t AliAnalysisUtils::IsFirstEventInChunk(AliVEvent *event)
```

- vertex selecton:

- ```
Bool_t AliAnalysisUtils::IsVertexSelected2013pA(AliVEvent *event)
with number of contributor > 2 and $v_z < 10$ cm;
```
- pileup rejection:

```
Bool_t AliAnalysisUtils::IsPileUpEvent(AliVEvent *event)
with the default cut values.
```

  - centrality QA = 0, V0A and ZNA are used as the centrality (or event multiplicity) estimators.

Table 1 shows the number of selected events in 7 event multiplicity bins.

| 0 – 5% | 5 – 10% | 10 – 20% | 20 – 40% | 40 – 60% | 60 – 80% | 80 – 100% |
|--------|---------|----------|----------|----------|----------|-----------|
| xxxxx  | xxxxxx  | xxxxxx   | xxxxxx   | xxxxxx   | xxxxxx   | xxxxxx    |

**Table 1:** Number of selected events in 7 event multiplicity bins with V0A centrality estimator in data.

## 2.2 MC

There are two sets of MC simulations have been used in this analysis:

- DPMjet simulations: for the  $V^0$  efficiency calculations and  $\Lambda$  ( $\bar{\Lambda}$ ) feeddown correction;
- PYTHIA simulations: used to build the detector response matrix for jets.

The details for each of the simulation sample are listed in the following.

### 2.2.1 *DPMjet simulations*

- p–Pb collisions at  $\sqrt{s_{NN}} = 5.02$  TeV;
- 12 runs(195344, 195346, 195351, 195389 195390, 195391, 195478, 195479 195480, 195481, 195483, 195482) in LHC13b4\_efix\_px ( $x$  from 1 to 4);
- events are selected by the same criteria as in data.

Table 2 shows the statistics in DPMjet simulations.

| 0 – 5% | 5 – 10% | 10 – 20% | 20 – 40% | 40 – 60% | 60 – 80% | 80 – 100% |
|--------|---------|----------|----------|----------|----------|-----------|
| xxxxx  | xxxxxx  | xxxxxx   | xxxxxx   | xxxxxx   | xxxxxx   | xxxxxx    |

**Table 2:** Number of selected events in 7 event multiplicity bins with V0A centrality estimator in DPMjet simulations.

### 2.2.2 *PYTHIA simulations*

- pp collisions at  $\sqrt{s} = 5.02$  TeV;
- data sample: LHC13b4 with LHC13b anchors;
- a Lorentz boost has to be applied for the rapidity shift in p–Pb system;
- events generated in 10  $p_T$ -hard bins:

$$[5, 11, 21, 36, 57, 84, 117, 152, 191, 234, \infty] \text{ (in } GeV/c\text{).} \quad (1)$$

### 3 Inclusive V<sup>0</sup>s Analysis: Comparison the PWG-LF Results

The strategy of the inclusive V<sup>0</sup> analysis is described in [1, 2]. In the following, a short summary about the details of the inclusive V<sup>0</sup> analysis as well as some general discussions will be given in the first three parts of this section. Then, the comparisons of the inclusive V<sup>0</sup> spectra between LF analysis and this analysis will be presented. At final, we will claim that, the discrepancy between the results in LF analysis and this analysis is mainly caused by the event selection criteria used in LF analysis and JE framework are different.

#### 3.1 Event selection of inclusive V<sup>0</sup> analysis

The event selection in the inclusive V<sup>0</sup> analysis [1, 2] is not exactly the same as that in EMCAL jet framework, the differences are:

- this analysis is based on AOD (as shown in section 2.1) and LF analysis is based on ESD;
- in this analysis, the event vertex is selected by using the pA 2013 vertex selection method in **AliAnalysisUtils**, this method requires the event should have the stable reconstructed vertex with TPC tracks, but this requirement is removed in the vertex selection criteria in LF analysis:

```
AliESDEvent *lESDevent = dynamic_cast<AliESDEvent*>(InputEvent());
const AliESDVertex *vertex = lESDevent->GetPrimaryVertexTracks();

Bool_t fHasVertex = kFALSE;
if (vertex->GetNContributors()<1) {
 vertex = lESDevent->GetPrimaryVertexSPD();
 if (vertex->GetNContributors()<1)
 fHasVertex = kFALSE;
 else
 fHasVertex = kTRUE;

 Double_t cov[6]={0};
 vertex->GetCovarianceMatrix(cov);
 Double_t zRes = TMath::Sqrt(cov[5]);

 TString vtxTyp = vertex->GetTitle();
 if (vtxTyp.Contains("vertexer:Z") && (zRes>0.25)) fHasVertex = kFALSE;
} else {
 fHasVertex = kTRUE;
}
```

- no pileup rejection in the LF analysis.

Figure 1 shows the ratios between the number of events with the given selection cuts in both AOD and ESD. The "default" cuts are the event trigger selection and centrality QA. These two cuts are the same in both LF analysis and this analysis. In the left panel of figure 1, the ratios are built between the results with the additional vertex selections and the default one. The pileup rejection is added in the ratios in the right panel of figure 1. The comparisons show that, the JE vertex selection rejects more events in the peripheral collisions than the LF vertex selection. And with a given vertex selection, the difference between AOD and ESD is small. This difference can be caused by the definitions of the primary vertex in AOD and that in ESD are different. Anyhow, the effect of the pileup rejection is small in LHC13b and LHC13c periods. And it is not expected to change the final results dramatically.

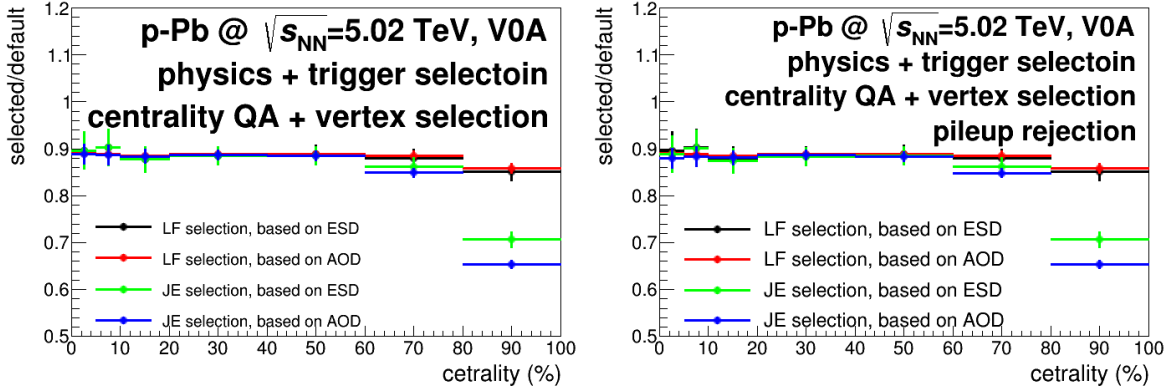


**Fig. 1:** Comparison of the LF and JE event selection criteria, see the texts for the details.

### 3.2 $V^0$ candidate selection

In both data and MC, the online  $V^0$ s are used in the analysis.

| selection                       | value                                         |
|---------------------------------|-----------------------------------------------|
| $V^0$ 2D decay radius           | in [0.5, 200] cm                              |
| negative track DCA to PV        | $> 0.06$ cm                                   |
| positive track DCA to PV        | $> 0.06$ cm                                   |
| DCA between $V^0$ daughters     | $< 1\sigma$                                   |
| $\cos \theta_{\text{pointing}}$ | $> 0.97$ ( $K_S^0$ ), $> 0.995$ ( $\Lambda$ ) |

**Table 3:** Default cuts for  $V^0$  decay topological selection.

| selection                          | value       |
|------------------------------------|-------------|
| track Kink index                   | $< 1$       |
| $ \eta $                           | $< 0.8$     |
| TPC refit flag                     | kTRUE       |
| number of crossed rows in TPC      | $> 70$      |
| number of findable rows in TPC     | $> 0$       |
| crossed rows / findable rows ratio | $> 0.8$     |
| TPC $dE/dx$                        | $< 5\sigma$ |

**Table 4:** Default selection cuts for  $V^0$  daughter tracks.

In data, the  $V^0$  candidates are selected by several set of cuts:

- $V^0$  secondary vertex reconstruction with  $\chi^2 < 33$ ;
- topological selection;
- daughter track selection;
- proper lifetime ( $mL/p$ ): default value for  $K_S^0$  ( $\Lambda$ ) is  $< 20$  cm ( $< 30$  cm);
- invariant mass restriction (as a function of  $V^0 p_T$ ):
  - $K_S^0$ :
  - \* upper band:  $0.563707 + 0.0114979 \times p_T$ ,

- \* lower band:  $0.430006 - 0.0110029 \times p_T$ ,
- $\Lambda$  and  $\bar{\Lambda}$ :
  - \* upper band:  $1.13688 + 0.00527838 p_T + 0.084222 \times \exp(-3.80595 p_T)$ ,
  - \* lower band:  $1.09501 - 0.00523272 p_T - 0.075269 \times \exp(-3.46339 p_T)$ ;
- competing V<sup>0</sup> rejection:
  - K<sub>S</sub><sup>0</sup>:  $|M_{p\pi^-} - M_\Lambda| > 0.005 \text{ GeV}/c^2$  and  $|M_{\bar{p}\pi^+} - M_{\bar{\Lambda}}| > 0.005 \text{ GeV}/c^2$ ,
  - $\Lambda$  and  $\bar{\Lambda}$ :  $|M_{\pi^+\pi^-} - M_{K_S^0}| > 0.01 \text{ GeV}/c^2$ .

The default cut values for the V<sup>0</sup> decay topology and V<sup>0</sup> daughter tracks are listed in table 3 and 4.

In MC, the reconstructed V<sup>0</sup>s and the decay daughter tracks are identified by the MC truth information. To build the numerator of the efficiency, the V<sup>0</sup>s candidates are selected by using exactly the cuts as in data except the daughter track PID with dE/dx in TPC.

### 3.3 Analysis strategy

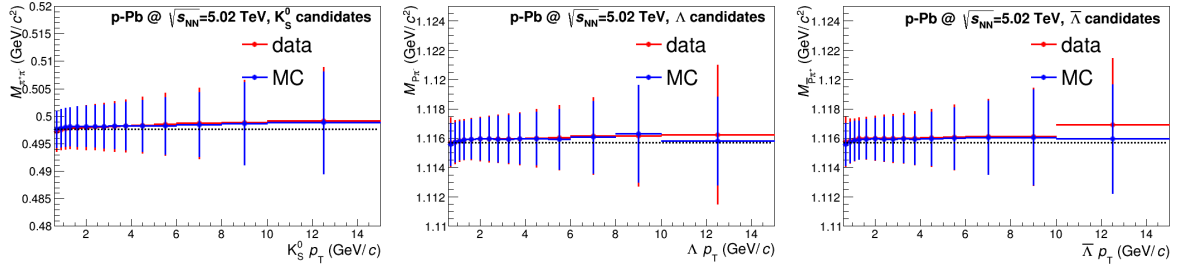


**Fig. 2:** The centre value and width of the V<sup>0</sup> candidates invariant mass distribution from the Gaussian fit. The results are shown as a function of  $p_T$  and they are obtained in 0 – 5% event multiplicity bin with the V0A estimator.

The strategy of the inclusive V<sup>0</sup> analysis includes the following steps:

- Extract raw spectra in data:
  1. fit V<sup>0</sup> invariant mass distribution with Gaussian plus a linear function in each  $p_T$  bin and extract the mean ( $M_{\text{mean}}$ ) and  $\sigma$  of the Gaussian;
  2. define the V<sup>0</sup> signal window as  $M_{\text{mean}} \pm N\sigma$  (the default option is  $N = 6$ );
  3. fit the combinatorial background in the side bands ( $[-2N\sigma + M_{\text{mean}}, -N\sigma + M_{\text{mean}}]$  and  $[N\sigma + M_{\text{mean}}, 2N\sigma + M_{\text{mean}}]$ ) and interpolate it into the signal window;
  4. subtract the interpolated background from the counts in signal window and extract the raw yield of V<sup>0</sup>s in each  $p_T$  bin.
- Build correction efficiency in MC:
  1. reproduce step 3 and 4 with the  $M_{\text{mean}}$  and  $\sigma$  extracted in data for the physical primary V<sup>0</sup>s at detector level in MC to define the numerator of the efficiency;
  2. the denominator of the efficiency is built by the physical primary particles at generation level;
  3. for  $\Lambda$  and  $\bar{\Lambda}$ , the  $\Xi$  feeddown component, which is evaluated by scaling the yield of feeddown  $\Lambda$  and  $\bar{\Lambda}$  in MC according to the measured  $\Xi$  spectra in data, have to be subtracted before the efficiency correction (details are described in [1]).

Figure 2 shows the centre value and width (the error bar) of the  $V^0$  candidates invariant mass distribution from the Gaussian fit<sup>1</sup> in  $0 - 5\%$  event multiplicity bin with the V0A estimator. The results are shown as a function of  $p_T$ . There is very good agreement for the centre points between the data and MC. In general, the width of the invariant mass distribution in MC is smaller than that in data. This is due to the invariant mass distribution of  $V^0$  candidates in MC is built by the MC truth  $V^0$  and there is no combinatorial background. The parameters obtained in data (the red curves) are used to build the  $p_T$ -dependent signal window and side bands for the background subtraction in both data and MC.

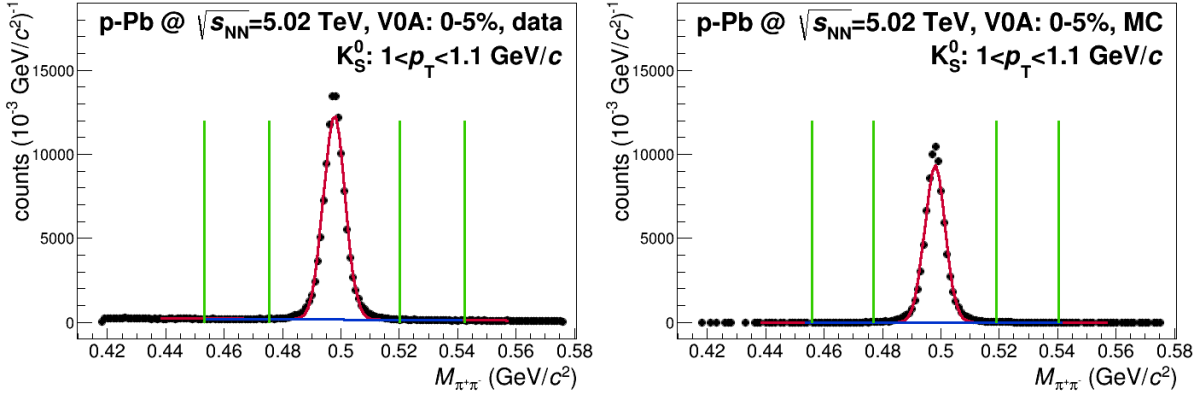


**Fig. 3:** Bin counting fits of the  $V^0$  invariant mass distributions in data (left) and in MC (right). The  $K_S^0$  candidates in  $1 < p_T < 1.1 \text{ GeV}/c$  and the most central collisions ( $0 - 5\%$ ) are chosen as an example.

As mentioned in section 3.2, the numerator of the efficiency is built by the MC truth  $V^0$ s and indeed, it does not contain the combinatory background. To reproduce the procedure of the combinatory background subtraction in MC is used to minimize the discrepancy between the data and MC. Figure 3 shows the bin counting fits of the  $K_S^0$  invariant mass distributions in data (left) and in MC (right) as an example. In each of the plot:

- the red line shows the Gaussian fit of the signal peak;
- the blue line is the built by interpolating the fit in the side bands into the signal window;
- the signal window and the side bands, which are defined by  $6\sigma$ , are separated by the green lines<sup>2</sup>.

One can notice that, the counts in the side bands in MC is non-vanished even all the  $V^0$ s are identified by the MC truth information. They are contributed by the  $V^0$ s which have large daughter track  $p_T$  resolution. And the interpolation of the bin counting fit in the side bands (the blue line) will also give a non-zero contribution in the signal region in the MC. In this case, the interpolated bin counting fit in data not only contains the combinatory background but also includes the contribution of the real  $V^0$ s which located in the side bands. Applying the background subtraction in data, it will subtract both the combinatory background and a fraction of real  $V^0$ s. To minimize this effect, the interpolated curve from the bin counting fit in the side bands was also subtracted in signal window in MC in the efficiency calculation.

Figure 4 shows the ratio between the interpolated curve in the signal window (the blue lines in figure 3) and the counts in the signal window after subtracting the interpolated curve in data (left) and in MC

<sup>1</sup>In data, the signal peak is fitted by the Gaussian plus a linear function and in MC the signal peak is fitted by the Gaussian alone.

<sup>2</sup>As also shown in figure 2, the width of the  $V^0$  invariant mass distribution in MC is smaller than that in data. Only the centre points and width extracted in data are used to calculate the efficiency.

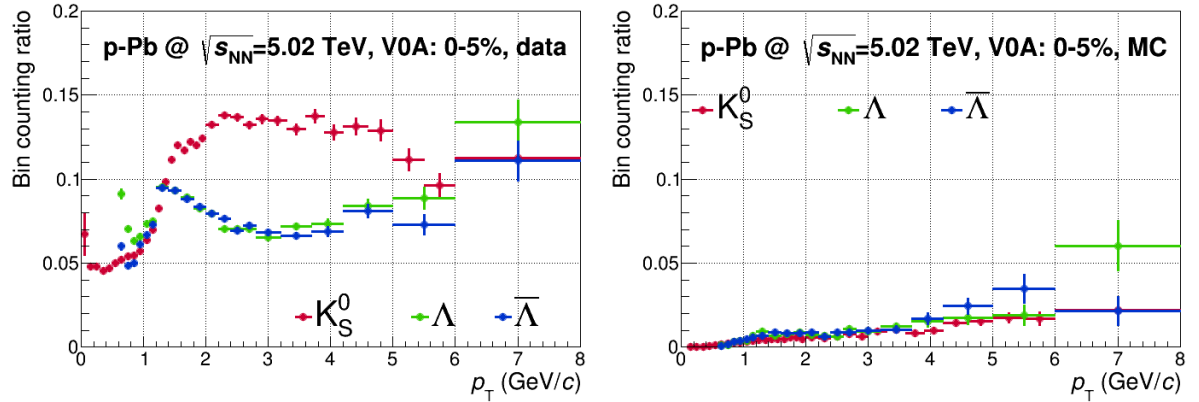


**Fig. 4:** The bin counting ratio for V<sup>0</sup>s as a function of  $p_T$  in data (left) and in MC (right). The results are obtained in 0 – 5% event multiplicity bin with V0A estimator. More details are in the texts.

(right):

$$R_{\text{Cbin}} = \frac{N_{\text{interp}}}{N_{\text{SW}} - N_{\text{interp}}}, \quad (2)$$

where,  $N_{\text{interp}}$  is the value of the interpolated curve and  $N_{\text{SW}}$  is the counts in the signal window. Here, we define it as the "bin counting ratio" ( $R_{\text{Cbin}}$ ). Indeed, this ratio is defined as the background-to-signal ratio of the inclusive V<sup>0</sup>s in data in [1]. In MC, this ratio has the non-vanish value and it is around 1% in low and intermediate  $p_T$  regions (the right panel of figure 4), but large fluctuations are found at high  $p_T$ . These fluctuations will be included in the systematic uncertainty of the final results (see the discussion in section 6.2.1).

### 3.4 Comparison to the LF results

In this analysis, to measure the production of V<sup>0</sup>s in jets, we derived the analysis task based on the EMCAL jet framework, which fills the jets and V<sup>0</sup>s into two independent tree branches, and the events are selected according the criteria in EMCAL jet framework. As the first step of this analysis, to validate our analysis code, we compared the V<sup>0</sup>s spectra in our measurement to those of the LF. As discussed in section 3.1, the event selection criteria in LF analysis and those in EMCAL jet framework are not the same and their effects are different, especially in the peripheral collisions (see figure 1). To ensure the comparison is done under the same conditions, we modified the EMCAL jet framework (privately) and used the same event and V<sup>0</sup> selection criteria as those in LF analysis. Our measurement is based on one run (run 195568,  $\sim 1.2^7$  events) in ESD. The LF results are from [3]. The V<sup>0</sup>s are selected in  $0 < y_{\text{CMS}} < 0.5$ .

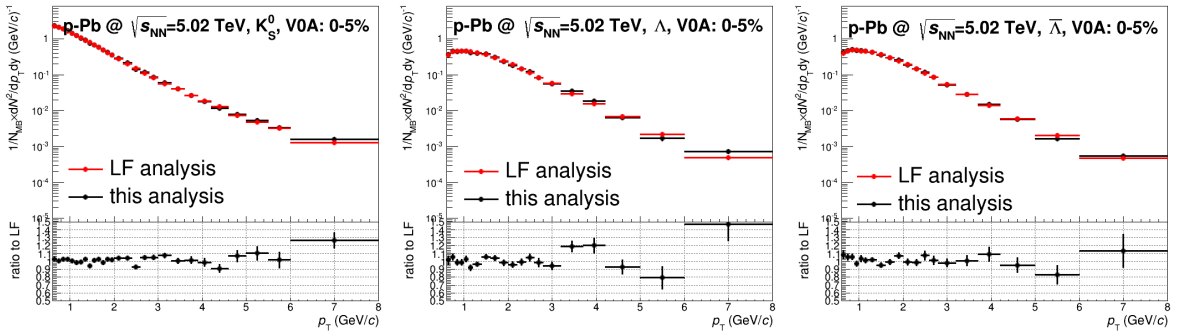


**Fig. 5:** Compare to LF results, 0 – 5%.

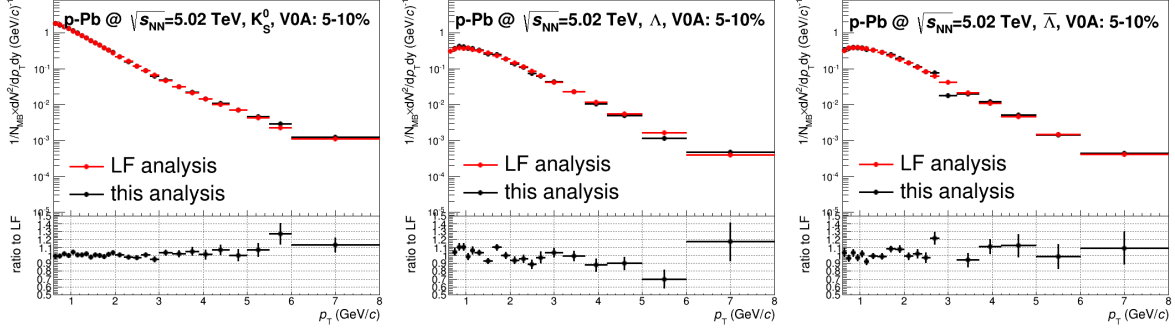


**Fig. 6:** Compare to LF results, 5 – 10%.

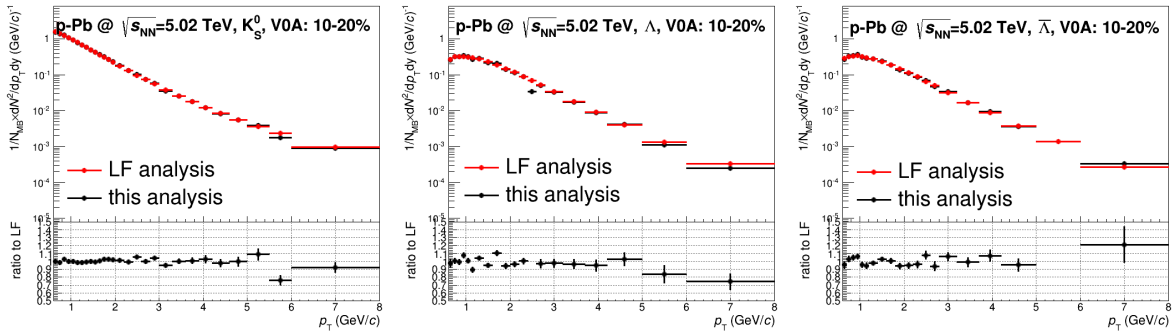


**Fig. 7:** Compare to LF results, 10 – 20%.

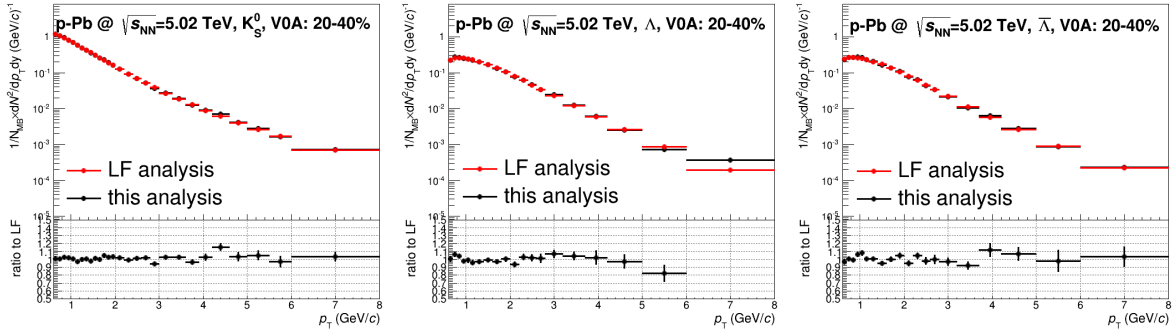
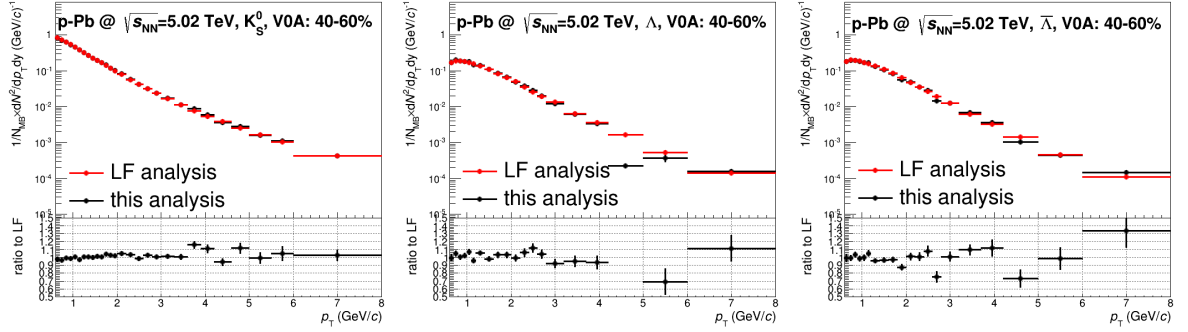


**Fig. 8:** Compare to LF results, 20 – 40%.

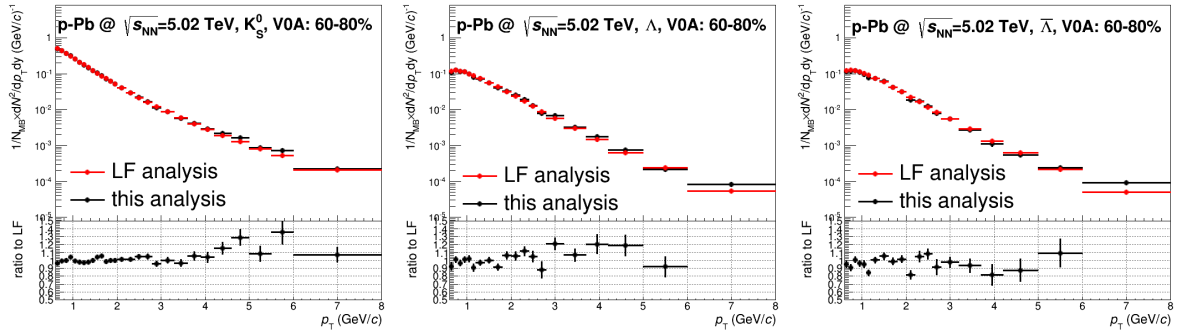
The comparisons are presented in seven event multiplicity bins, the results are shown in figure 5 to figure 11. These two analyses are consistent within the statistic errors in all event multiplicity bins.

Figure 12 to figure 17 are the comparisons of the results in LF and JE analyses. The same as figure 5 to figure 11, the LF results come from ref. [3]. But the results in this analysis is obtained with the JE event and selections and based on AOD. The two analyses are consistent in the central and semi-central collisions, but the deviation is found in the peripheral collisions.

This deviation in the peripheral collisions can be explained by the comparisons shown in figure 1. For more details, we compared the ratio of the per-event multiplicity of  $V^0$  candidates as a function of  $p_T$  with JE and LF event selections, respectively. The comparisons are shown in figure 18 (for central collisions) and in figure 19 (for peripheral collisions) with the VOA event multiplicity estimator. The  $V^0$  candidates are selected by the cuts defined in section 3.2, the cut on the invariant mass is also applied but without



**Fig. 9:** Compare to LF results, 40 – 60%.



**Fig. 10:** Compare to LF results, 60 – 80%.

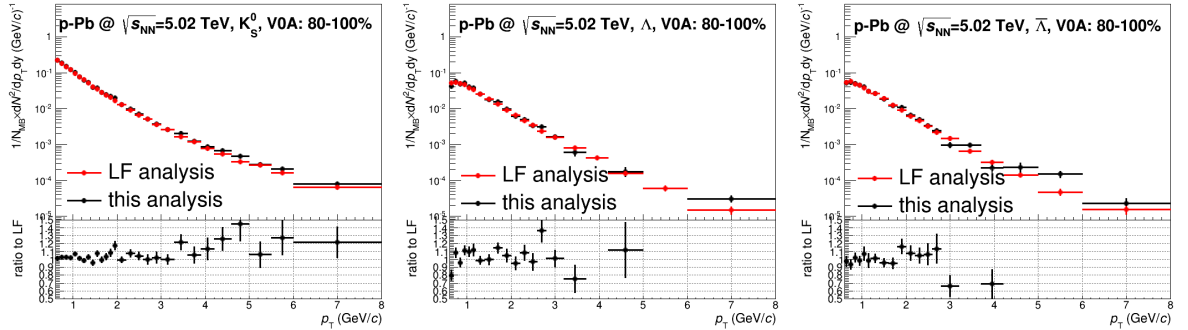


**Fig. 11:** Compare to LF results, 80 – 100%.

the combinatory background subtraction. In the central collisions (0 – 10%, figure 18), the JE analysis LF analysis give the exactly the same results which is consistent with the conclusion in figure 1. But in the peripheral collisions, the  $V^0$  mutliplicity in JE analysis is higher than that in the LF analysis. The tighter vertex selection criteria implemented in the EMcal jet framework rejects the lower multiplicity events w. r. t. the LF analysis and makes the  $V^0$  spectra in this analysis is systematically higher than those in the LF analysis<sup>3</sup>.

<sup>3</sup>We have discussed the discrepancy in the peripheral collisions between these two analysis with the LF people. And they claimed that, this discrepancy could be caused by the cut of the  $\cos \theta_{\text{pointing}}$  (see section 3.2). Due to when they first compared their  $K^0_S$  results to the charged Kaons, they found the very similar deviation in the peripheral collisions. According to this, they suggested to use the  $p_T$ -dependent  $\cos \theta_{\text{pointing}}$  cut to decrease the discrepancy. But if the discrepancy between our analysis and LF analysis is mainly caused by the effect of the  $\cos \theta_{\text{pointing}}$  cut, it has to be also found in the ESD based analysis, and this is not the case.

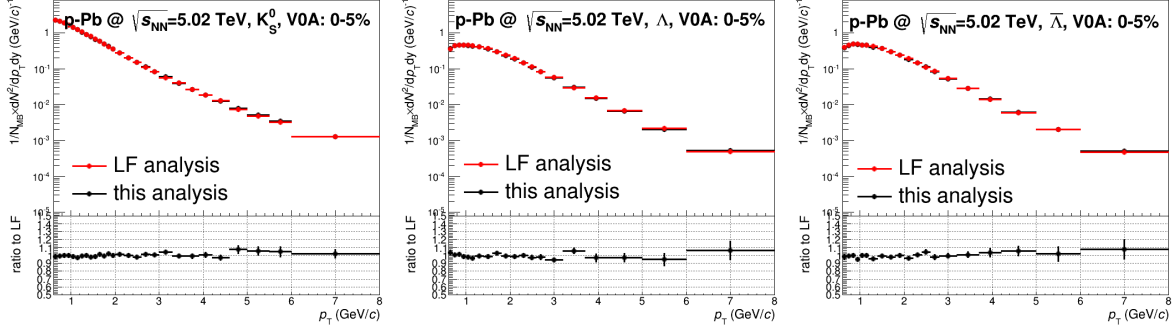


**Fig. 12:** Compare to LF results, 0 – 5%.  $V^0$  sepectra in this analysis is obtained with the JE event selection criteria.

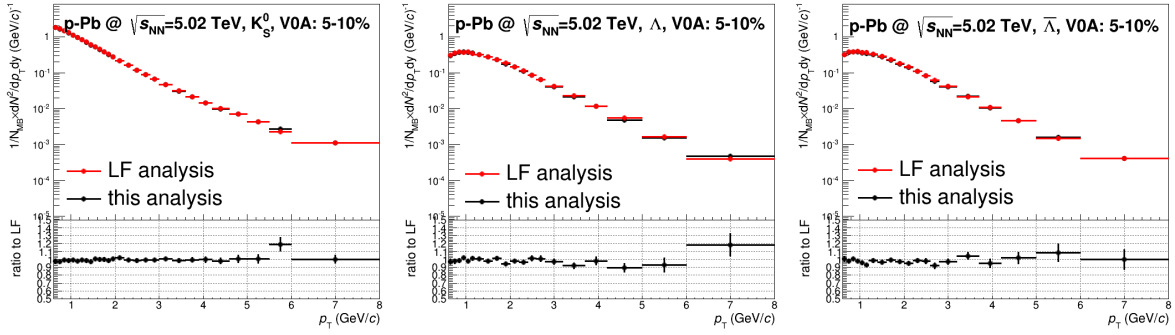


**Fig. 13:** Compare to LF results, 5 – 10%.  $V^0$  sepectra in this analysis is obtained with the JE event selection criteria.

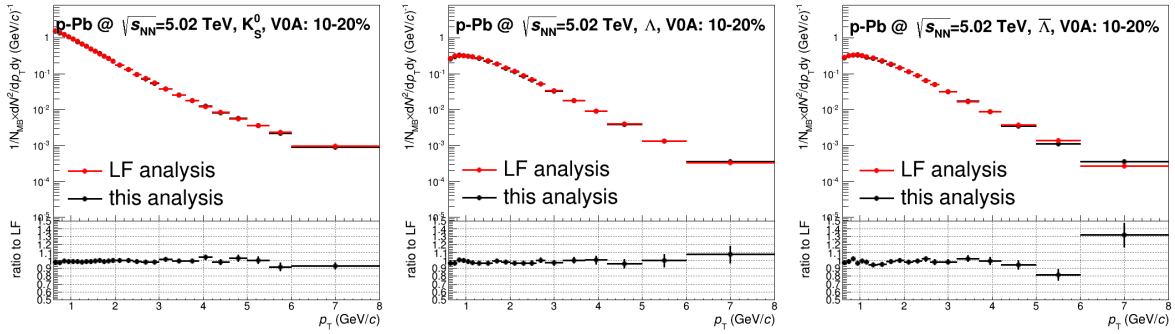


**Fig. 14:** Compare to LF results, 10 – 20%.  $V^0$  spectra in this analysis is obtained with the JE event selection criteria.

Indeed, the final results in this analysis is focused on the  $\Lambda$ -to- $K_S^0$  ratio in jets. It is interesting to see how the effects of the event selections on the this ratio of the inclusive  $V^0$ s. The ratio of  $(\Lambda + \bar{\Lambda})/2K_S^0$  in four event multiplicity bins with the input spectra come from figure 12 to figure 17 are compared in figure 20. The error bar in the LF results corresponds the quadratically combined statistic and systematic uncertainties. Despite the difference in the spectra, the ratios of  $(\Lambda + \bar{\Lambda})/2K_S^0$  in this analysis are consistent with those in LF analysis within errors from the central to the peripheral collisions. The small bin-by-bin discrepancy between this two analyses is caused by the bin counting fitting [1] to extract the number of signals and to build the efficiency in the fine bins of  $p_T$ . This procedure is sensitive to the analysis details.

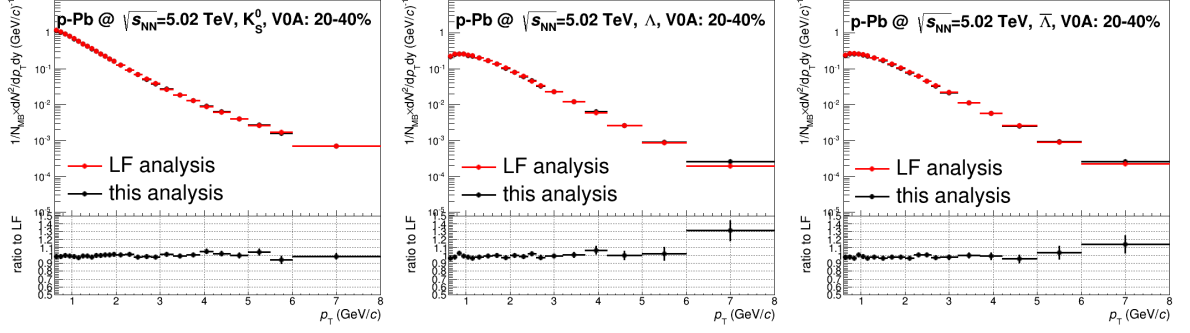


**Fig. 15:** Compare to LF results, 20 – 40%. V<sup>0</sup> spectra in this analysis is obtained with the JE event selection criteria.

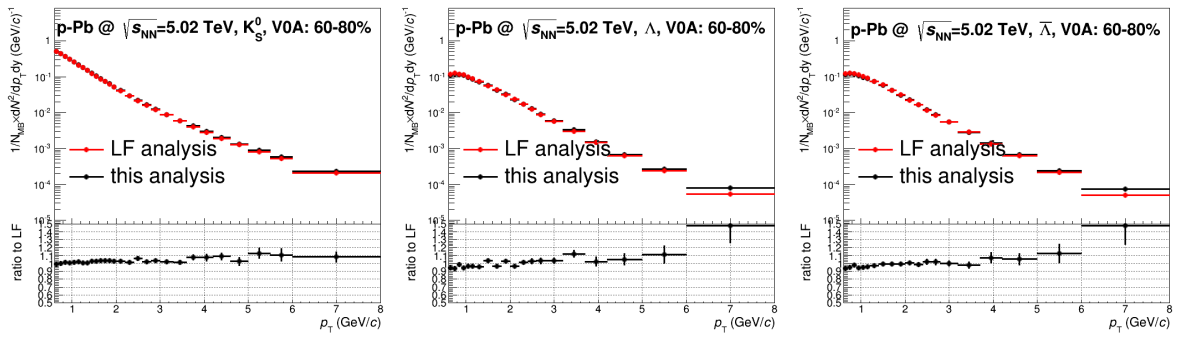


**Fig. 16:** Compare to LF results, 60 – 80%. V<sup>0</sup> spectra in this analysis is obtained with the JE event selection criteria.

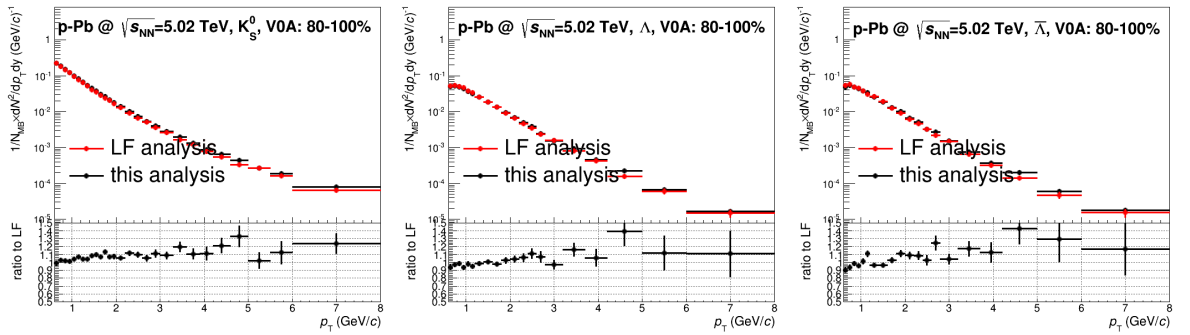


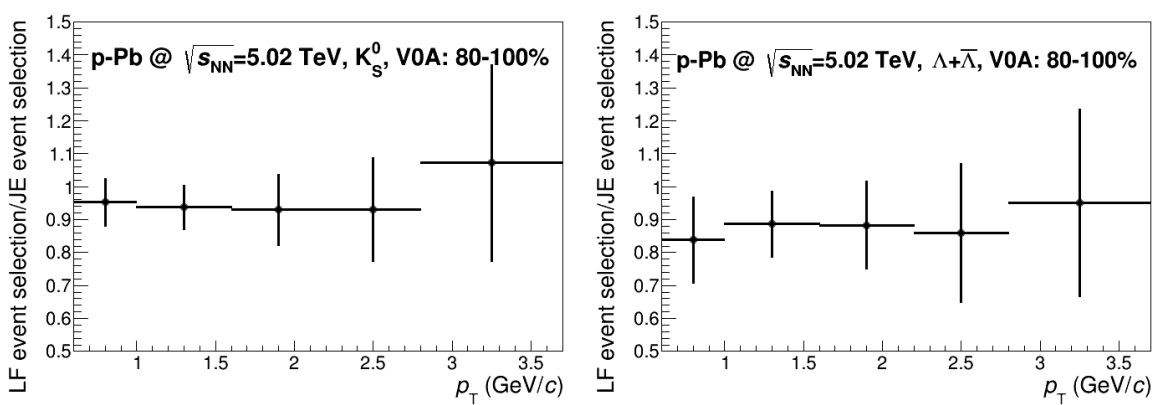
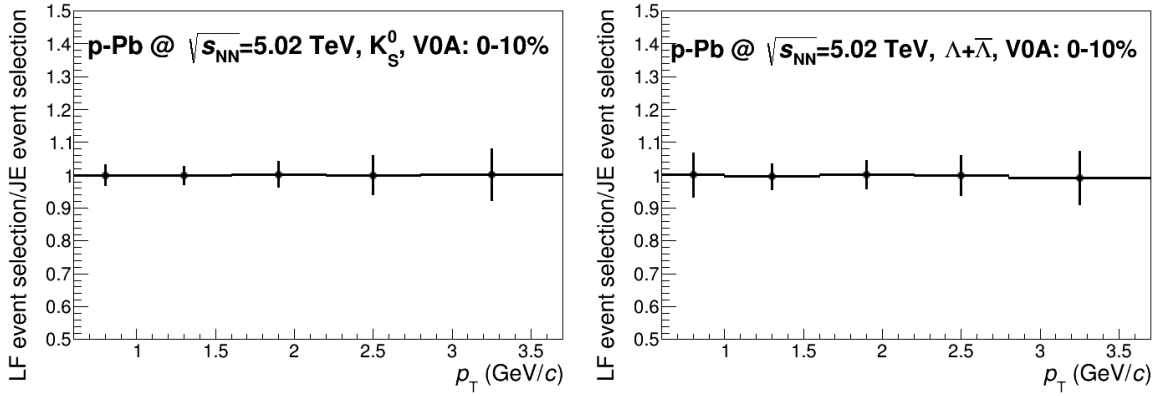
**Fig. 17:** Compare to LF results, 80 – 100%. V<sup>0</sup> spectra in this analysis is obtained with the JE event selection criteria.

## 4 Charged Jets Analysis

### 4.1 Inclusive jets reconstruction

In this work, the charged jets are obtained by the strategy used in [4]. The signal jets are reconstructed by the following criteria:

- charged track selection:
  - acceptance:  $p_T > 0.15$  GeV/c and  $|\eta| < 0.9$  (TPC acceptance),
  - hybrid track filter: the same as the that used in Pb–Pb collision taken in 2011;



- jet reconstruction:
  - jet finder: anti- $k_T$ ,  $R_{jet} = 0.4$ , 0.3 and 0.2,
  - acceptance:  $|\eta| < 0.5$ .

## 4.2 Jet background density

The jet background density [5, 6] is estimated by the jet constituents reconstructed by  $k_T$  algorithm with the same track and acceptance cuts as the signal jets. To minimize the local track density fluctuations in p–Pb collisions, a method derived from the so called CMS method [7] (see also [4] for the implementation in ALICE) is adopted in this analysis. This method includes the following steps:

- calculate the jet background density with  $k_T$ -jets according to the median approach [5]:

$$\rho_{bkg} = \text{median}\left\{\frac{p_T^{\text{jet}}}{A_{\text{jet}}}\right\}; \quad (3)$$

where,  $A_{\text{jet}}$  is the jet area defined in [6];

- scale  $\rho_{bkg}$  with the ratio between the area covered by jets and the event acceptance in  $\eta - \phi$  plane:

$$\rho_{\text{CMS}} = \frac{\text{area covered by jets}}{\text{total area}} \rho_{bkg}; \quad (4)$$

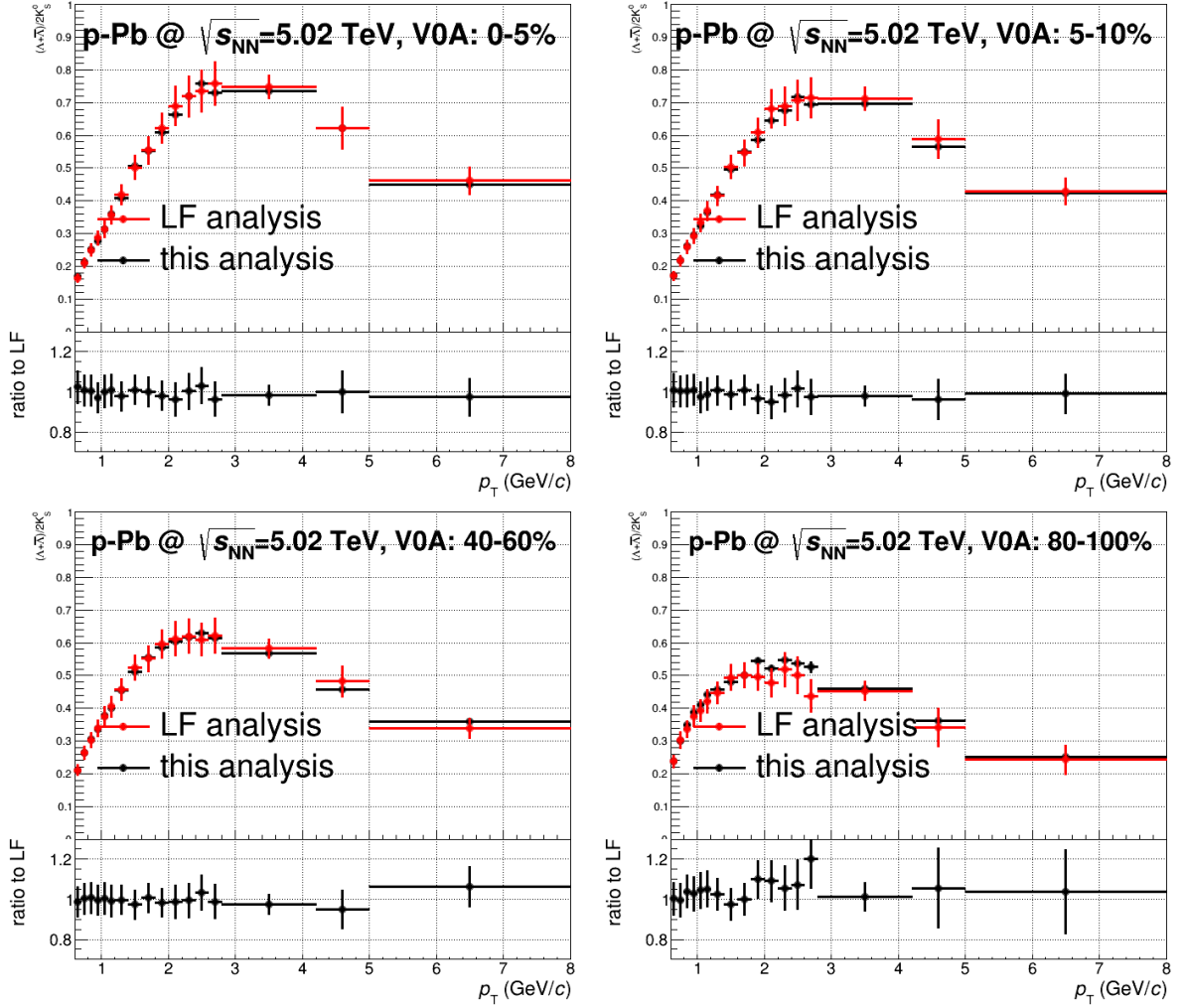


**Fig. 20:** The comparison for the ratio of  $(\Lambda + \bar{\Lambda})/2K_s^0$  in LF analysis and this analysis in 7 event multiplicity bins. The input spectra are from figure 12 to figure 17.

- to further refined the CMS method in p–Pb collisions, the  $k_T$ -jets that share tracks with the signal jets (anti- $k_T$  jets) are removed in the calculation of the background density in eq. (3) and the area scale factor in eq. (4).

Figure 21 shows the 2D distributions of  $\rho_{\text{CMS}}$  vs. event multiplicity (left) and acceptance correction factor vs. event multiplicity (right). The centrality estimator is V0A. As expected, both the jet background density and the acceptance correction factor decreases with the event multiplicity.

After obtaining the jet background density, the estimated jet  $p_T$  is given by correcting the measured jet  $p_T$  with the background:

$$p_T^{\text{esti}} = p_T^{\text{meas}} - \rho \cdot A_{\text{jet}}, \quad (5)$$

where,  $p_T^{\text{meas}}$  is the measured jet  $p_T$  and  $A_{\text{jet}}$  is the jet area, jet background density is given by the  $\rho_{\text{CMS}}$  in eq. (4).

The measured jet  $p_T$  spectrum and the estimated jet  $p_T$  spectrum in three event multiplicity bins are compared in figure 22 (with  $R_{\text{jet}} = 0.4$ ) and figure 23 (with  $R_{\text{jet}} = 0.2$ ), respectively. The discrepancy between them decreases when jet  $p_T$  increasing.

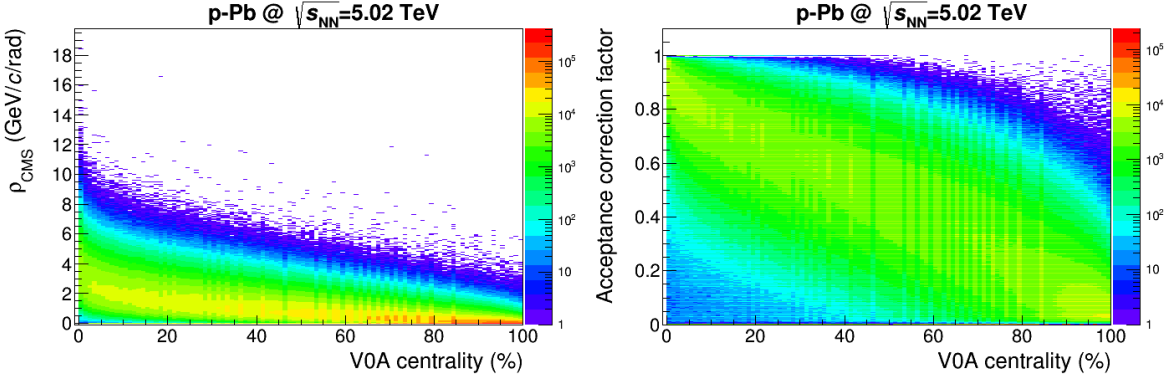


**Fig. 21:** Left: 2D distribution of  $\rho_{\text{CMS}}$  vs. event multiplicity; right: 2D distribution of the acceptance correction factor vs. event multiplicity. The centrality estimator is V0A.

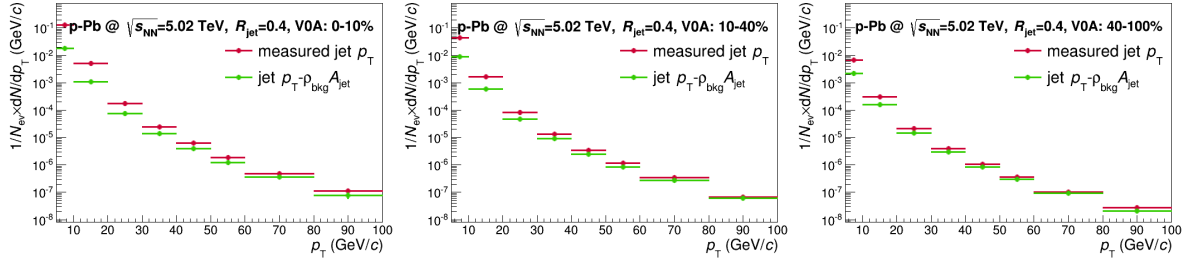


**Fig. 22:** The comparison of measured jet  $p_T$  spectrum and the corrected jet  $p_T$  spectrum in three event multiplicity bins with V0A estimator. The jets are measured with  $R_{\text{jet}} = 0.4$ .

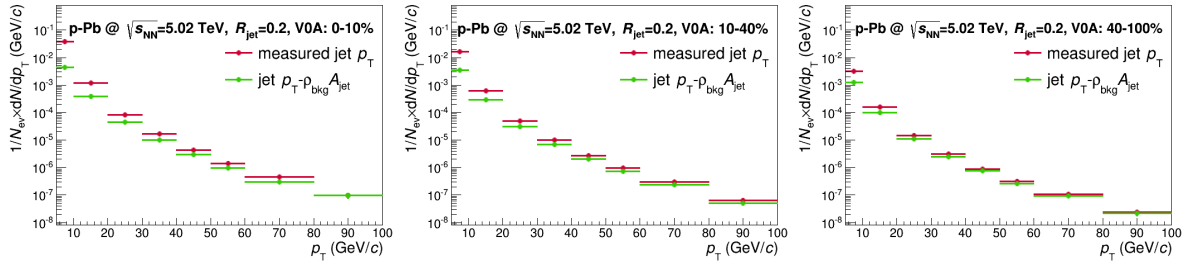


**Fig. 23:** The comparison of measured jet  $p_T$  spectrum and the corrected jet  $p_T$  spectrum in three event multiplicity bins with V0A estimator. The jets are measured with  $R_{\text{jet}} = 0.2$ .

Due to the acceptance of the V0A ( $2.8 < \eta < 5.1$ ) is closer to the jet acceptance (the jet constituents are selected in  $|\eta| < 0.9$ ) and it has the correlations between the reconstructed jets at the mid-rapidity. To decrease the acceptance correlations as well as to study the systematic uncertainty on different centrality estimators, the ZNA ( $|\eta| \sim 8$ ) is also used in this analysis. Figure 24 shows the comparison of corrected jet  $p_T$  spectra obtained with the V0A centrality estimator and those obtained with the ZNA centrality estimator in three event multiplicity bins. The results with  $R_{\text{jet}} = 0.4$  are presented in the upper three plots and the results with  $R_{\text{jet}} = 0.2$  are presented in the lower three plots. The discrepancy between the two centrality estimators is visible in the central (0 – 10%) and peripheral (40 – 80%) collisions and they give almost the same results in the semi-central collisions (10 – 40%).

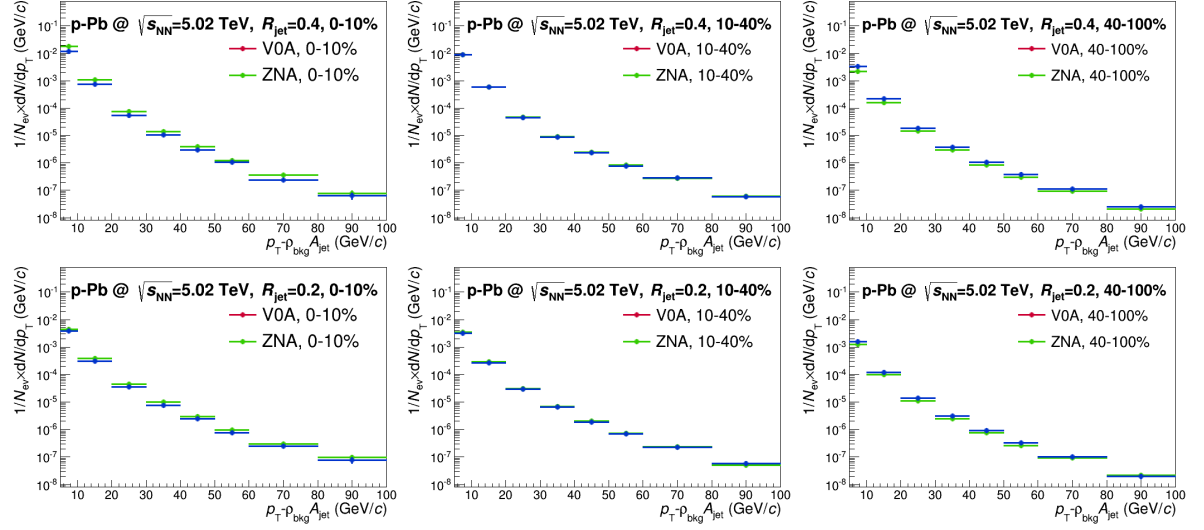


**Fig. 24:** The comparison of corrected jet  $p_T$  spectra obtained with the VOA centrality estimator and those obtained with the ZNA centrality estimator in three event multiplicity bins. The jets are measured with  $R_{\text{jet}} = 0.4$  (upper) and  $R_{\text{jet}} = 0.2$  (lower).

### 4.3 Background fluctuations

The fluctuations of jet background density, which illustrated by the observable  $\delta p_T$ , is evaluated by using the random cone method [8]. The approaches are:

- throw the cones with same radius as the jet and randomized  $\eta$  and  $\phi$  in the jet acceptance in each event;
- calculate the  $\delta p_T$ :

$$\delta p_T = \sum_{\text{in cone}} p_T - \rho \cdot A_{\text{cone}}, \quad (6)$$

where, the sum runs the selected tracks in the cone,  $A_{\text{cone}} = \pi R_{\text{jet}}^2$  is the cone size. The  $\rho_{\text{CMS}}$  is used in calculation in this analysis.

With this definition, the non-zero value of  $\delta p_T$  shows the difference between the track  $p_T$  that in a random chosen and the expected background of jets. Statistically, it gives the fluctuations of the background. Another source for non-zero  $\delta p_T$  given by the cone can overlap with the jets. It is not problematic since jets can also overlap each other. To account for this, in the calculation of the  $\delta p_T$ , the random cones overlapping with the leading jet is rejected with a probability given by:

$$p = \frac{1}{N_{\text{coll}}}, \quad (7)$$

where  $N_{\text{col}}$  is the average number of hard collisions per minimum bias event. With the partial exclusion,  $R_{\text{pPb}}$  of charged jets is changed by less than 1% [4]. Figure 25 shows the  $\delta p_T$  distribution in this analysis, the RMS of this distribution is  $\sim 1 \text{ GeV}/c$ .

### 4.4 Detector response matrix

The single track efficiency and resolution also affects the resolution of the reconstructed jet  $p_T$ . These effects are described by the detector response matrix, which is built as:

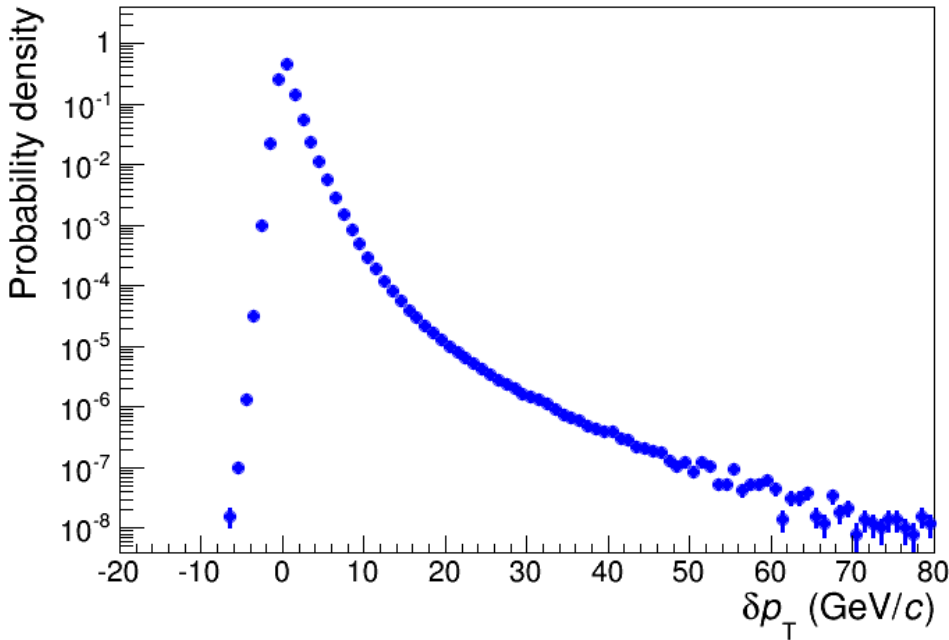


**Fig. 25:** The  $\delta p_T$  distribution obtained by the random cone approach with the  $\rho_{\text{CMS}}$ .

- simulate events with the realistic detector configurations as those in data;
- run the jet finder at particle level (over the generated particles, which have no detector effect);
- represent the jet finder at the detector level (over the reconstructed tracks);
- match the jets at particle level and detector level with  $\Delta R < 0.1$  in the  $\eta - \phi$  plan;
- the detector response matrix is built as the correlations of the  $p_T$  for jets at particle level and that at detector level.

In this analysis, the detector response matrix is obtained from LHC13b4 simulations which are introduced in section 2.2.2. Figure 26 shows the detector response matrix used in this analysis.

## 5 Production of $V^0$ s in Jets

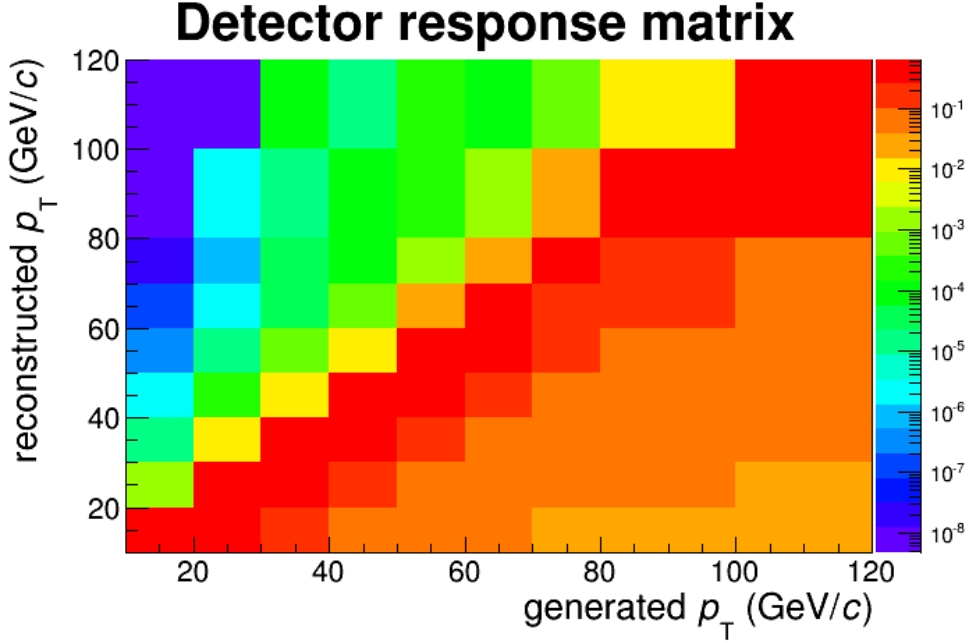
### 5.1 Analysis strategy

#### 5.1.1 Acceptance

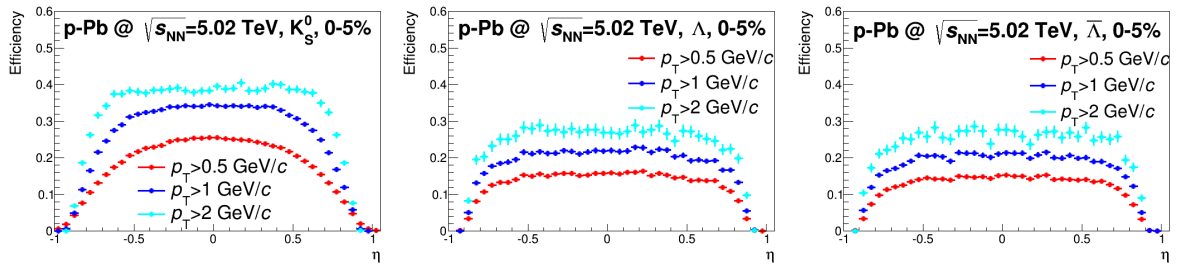
The details about the inclusive  $V^0$ s analysis is described in section 3. And the inclusive  $V^0$ s are selected in  $0 < y_{\text{cms}} < 0.5$ . To match the  $V^0$ s with the jets, here we selected the  $V^0$ s on  $\eta - \phi$  plan to get the uniform acceptance definition for both  $V^0$ s and jets.

Figure 27 and 28 shows the efficiency of inclusive  $V^0$ s as a function of  $\eta$  in the central collisions (0 – 10%) and in MB events (0 – 100%), respectively. Due to the  $V^0$  daughters are selected in  $|\eta| < 0.8$ , the efficiency is decreased when closing to this kinematics bound. To minimize the bound effect on the  $V^0$  candidates selection, we restricted the  $V^0$ s in and jets in:

- $V^0$ s:  $|\eta| < 0.75$ ;
- jets:  $|\eta| < \eta_{V^0}^{\max} - R_{\text{jet}}$  ( $|\eta_{\text{jet}}| < 0.35$  with  $R_{\text{jet}} = 0.4$  and  $|\eta_{\text{jet}}| < 0.55$  with  $R_{\text{jet}} = 0.2$ ).



**Fig. 26:** The  $\delta p_T$  distribution obtained by the random cone approach with the  $\rho_{\text{CMS}}$ .



**Fig. 27:** Efficiency of inclusive  $V^0$ s as a function of  $\eta$  in central collisions (0 – 5%, with V0A centrality estimator).

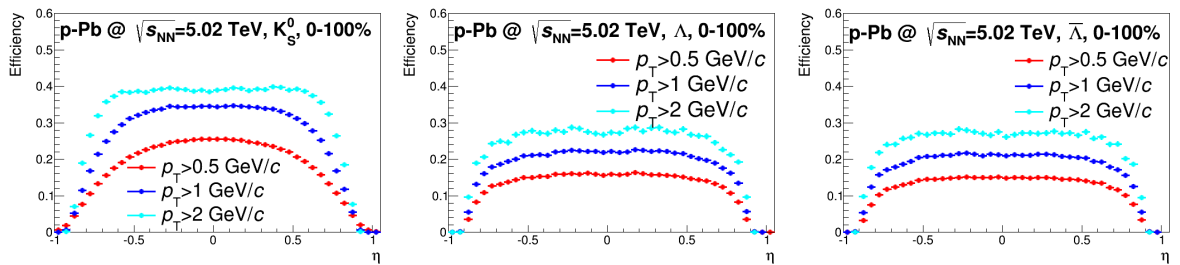


**Fig. 28:** Efficiency of inclusive  $V^0$ s as a function of  $\eta$  in MB event (0 – 100%, with V0A centrality estimator).

The reducing of the jet acceptance is also useful to avoid the bound effect in jet reconstruction.

### 5.1.2 $V^0$ -jet matching

The first task to obtain the yield of  $V^0$ s produced inside the jet cone is to extract the number of  $V^0$ s matched to the jets. This is done with the following steps:

1. select the  $V^0$  candidates with the cuts defined in section 3.2, as discussed in section 5.1.1, the  $V^0$

candidates are selected in the acceptance of  $|\eta| < 0.75$ ;

2. match the  $V^0$ s candidates and jets according to the geometry cut:

$$\Delta R_{V^0-jet} < R_{jet}, \quad (8)$$

where,  $\Delta R_{V^0-jet}$  is the distance between the  $V^0$  and jet axis in  $\eta - \phi$  plane;

3. fill the invariant mass distribution of the  $V^0$  candidates matched to the jets in each  $V^0 p_T$  bin, then define the signal window and the side bands of the filled invariant mass distribution according to the mean and width from the **inclusive**  $V^0$  invariant mass distribution;
4. fit the counts in the side bands and interpolate the result into the signal window;
5. the number of  $V^0$ s matched to jets are obtained by subtracting the interpolated result from the counts in the signal window in each  $V^0 p_T$  bin.

The  $V^0$ s (or  $V^0$  candidates) which matched to the jets are named as the **JC  $V^0$ s** (or **JC  $V^0$  candidates**).

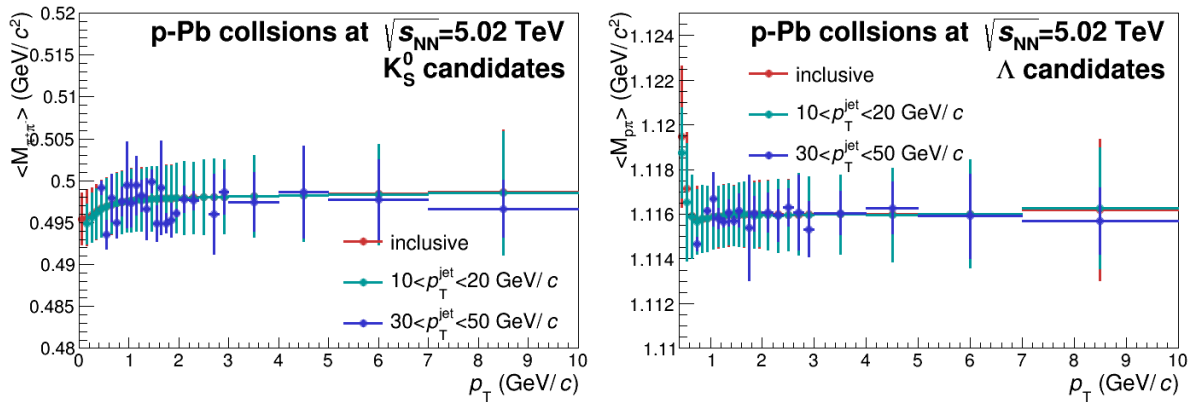


**Fig. 29:** The mean and width of  $V^0$  invariant mass distribution extracted by the Gaussian fit for the inclusive  $V^0$ s candidates and JC  $V^0$  candidates as a function of  $p_T$  in data.

Figure 29 shows the comparison of the mean and width of  $V^0$  invariant mass distribution extracted by the Gaussian fit for the inclusive  $V^0$ s candidates and JC  $V^0$  candidates as a function of  $p_T$  in data. Indeed, the mean and width in the  $V^0$  invariant mass distributions for the inclusive  $V^0$ s and JC  $V^0$ s are almost the same. But the large fluctuations caused by the less of the statistics are found in these two variables obtained from the the JC  $V^0$ s in the higher jet  $p_T$  bins. To avoid these statistic fluctuations, the number of JC  $V^0$ s is extracted by using the mean and width obtained in the inclusive  $V^0$  invariant mass distribution.

Due to the  $V^0$  candidates and the jets are reconstructed independently in this analysis. In eq. (8) a  $V^0$  candidate can match to more than one jet due to the jet area is not always as a regular circle. And this effect has to be considered when normalizing the JC  $V^0$ s to the corresponding number of jets (see section 5.3). To overcome the multiple countings in the normalization of the JC  $V^0$  sepectra, the following steps are used for the  $V^0 - \text{jet}$  matching:

- define a jet  $p_T$  threshold,  $p_T^{\min}$ ;
- for a given  $V^0$  candidate, made the loop over all the selected jets with  $p_T$  above the  $p_T^{\min}$  and in the corresponding jet  $\eta$  acceptance in the event and, tagged it as the JC  $V^0$  candidate if it can match with at least one selected jet in the event according to eq. (8).

### 5.1.3 Underlying V<sup>0</sup> estimation

To obtain the spectra of V<sup>0</sup>s produced in the jets, the V<sup>0</sup>s produced in the underlying events (**UE V<sup>0</sup>s**) have to be subtracted from the yield of JC V<sup>0</sup>s. The basic idea is to use the V<sup>0</sup>s outside the jet cone to estimate the density of the UE V<sup>0</sup>s inside jet cone. But there are two effects which bias the underlying V<sup>0</sup> evaluation:

- the V<sup>0</sup>s outside the selected jets could be matched with the excluded jets which are rejected by the  $p_T$  and  $\eta$  cuts of the jet selection;
- due to the detector response and the jet reconstruction efficiency, the physical jets associated to the V<sup>0</sup>s could be lost by the jet finder.

In this case, we use two different methods to estimate underlying V<sup>0</sup>s:

- V<sup>0</sup>s outside jet cone (**OC V<sup>0</sup>s**):

$$\Delta R_{V^0\text{-jet}} > R_{\text{cut}}, \quad (9)$$

where,  $R_{\text{cut}}$  is a given threshold of the distance between the V<sup>0</sup> and jet axis in  $\eta - \phi$  plane;

- V<sup>0</sup>s in events without any selected jet (**NJ V<sup>0</sup>s**).

According to the definitoin, the OC V<sup>0</sup>s are selected in the same event sample as the JC V<sup>0</sup>s and they can include both the V<sup>0</sup>s in the excluded jets and the physical jets lost by the jet finder, they have a strong correlation to the V<sup>0</sup>s produced in the jets. On the other hand, if the  $p_T$  threshold used to select the jet is low enough, we do not expect there would be a strong hard scattering in the NJ events, and the probability for the NJ V<sup>0</sup>s to match to the physical jets is lower and their correlations to the V<sup>0</sup>s produced in the jets is weaker.

In this analysis, the JC V<sup>0</sup>s and the OC V<sup>0</sup>s are selected in the two open jet  $p_T$  bins:  $p_T^{\text{jet}} > 10 \text{ GeV}/c$  and  $p_T^{\text{jet}} > 20 \text{ GeV}/c$ . The **corrected** jet  $p_T$  in eq. (5) is used for the jet selection. The NJ V<sup>0</sup>s are defined in the event without jet in **measured**  $p_T > 5 \text{ GeV}/c$ . The uncertainly on UE V<sup>0</sup> estimation is given by the difference between the OC and NJ V<sup>0</sup>s.

## 5.2 Efficiency

### 5.2.1 V<sup>0</sup> efficiency in MC

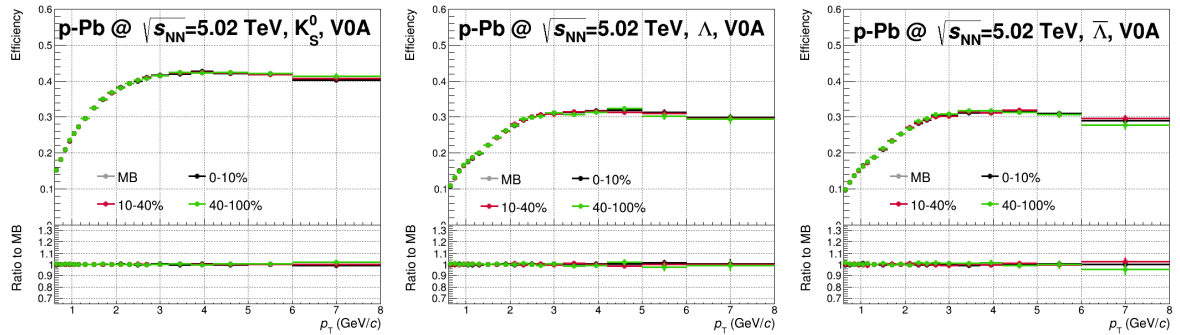


**Fig. 30:** Efficiency of inclusive V<sup>0</sup>s as a function of  $p_T$  in three event multiplicity bins with V0A centrality estimator.

Figure 30 shows the efficiency of the inclusive V<sup>0</sup>s as a function of  $p_T$  in three event multiplicity bins. The results are obtained with the strategy introduced in section 3.3. The ratio of the efficiency in each

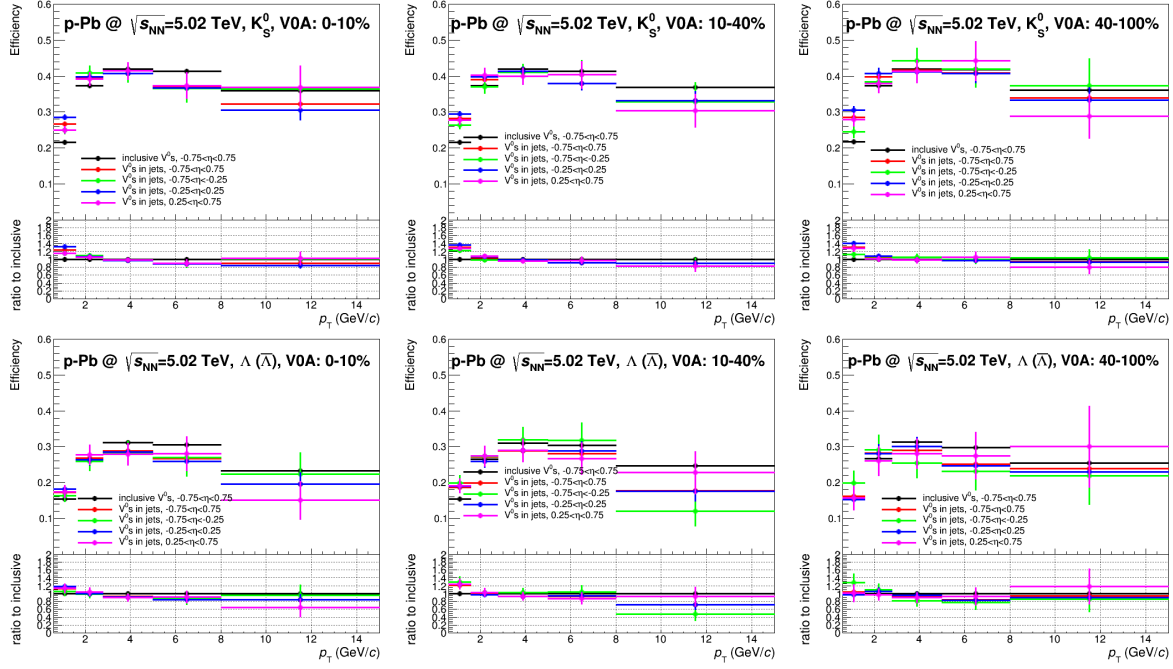
event multiplicity bins and that in the minimum-bias events (0 – 100%) is also presented in this figure. One can find that, the efficiency of inclusive  $V^0$ s is independent on the event multiplicity.

To implement the efficiency correction to the JC and OC  $V^0$ s one has to consider that, the efficiency of  $V^0$ s inside and outside jet cone could be different. As a testing, we used to the following steps to check the efficiency of JC  $V^0$ s in the simulations:

1. reconstruct and select the jets in the simulations at detector level (with the reconstructed tracks) with the same criteria as in data,
2. match the physical primary  $V^0$ s at particle level (the generated particles) to the reconstructed jets to build the denominator of the efficiency;
3. reproduce the steps in section 5.1.2 to obtain the number of JC  $V^0$ s at detector level and use it to build the numerator of the efficiency.

This procedure is summarized in [9]<sup>4</sup>.

As discussed in section 3.3, to build the numerator of the  $V^0$  efficiency, the interpolated result from the fit in the side bands has to be subtracted from the signal window. Due to the bin counting ratio of the inclusive  $V^0$ s in MC (as shown in the right panel of figure 4) is only  $\sim 1\%$ . At here, the bin counting subtraction of the JC  $V^0$ s in MC is done by applying the bin counting ratio of the inclusive  $V^0$ s. The uncertainty introduced by this procedure should have a order of 1%, especially, in the low and intermedia  $p_T$  regions.



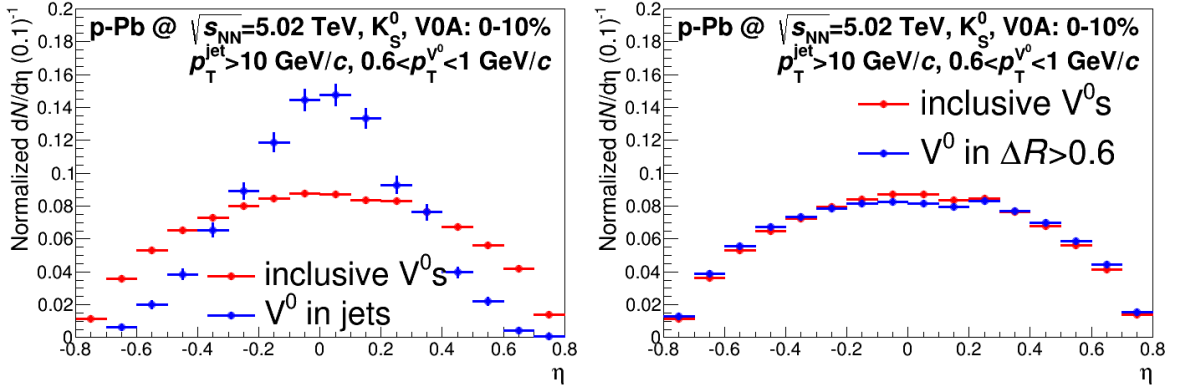
**Fig. 31:** Efficiency of  $V^0$ s in jets as a function of  $p_T$  in three event multiplicity bins in simulations. The results are obtained in  $p_T^{\text{jet}} > 10 \text{ GeV}/c$ .

Figure 31 shows the efficiency of  $V^0$ s with jets in  $p_T > 10 \text{ GeV}/c$ . The results are compared with those of the inclusive  $V^0$ s as well as the those obtained in three sub- $\eta$  bins. In general, the efficinceny of  $V^0$ s

<sup>4</sup>There are two strategies for the efficiency estimation of JC  $V^0$ s in MC are proposed in [9]. The procedure introduced in this note is corresponding to the second one.

in jets is  $\sim 20\%$  higher than that of inclusive V<sup>0</sup>s in low  $p_T$  region. At high  $p_T$ , the efficiency of V<sup>0</sup>s in jets is consistent with the efficiency of inclusive V<sup>0</sup>s. To deeply handle the efficiency correction of the JC and OC V<sup>0</sup>s, one has to understand the reason for the increasing of the efficiency JC V<sup>0</sup>s w. r. t. that of inclusive V<sup>0</sup>s in the low  $p_T$  region.

### 5.2.2 $\eta$ modified V<sup>0</sup> efficiency



**Fig. 32:** Normalized  $\eta$  distribution of  $K_S^0$  in jets (left) and OC  $K_S^0$  with  $\Delta R > 0.6$  (right) in data. The results are compared to the  $\eta$  distribution of inclusive and  $K_S^0$ .

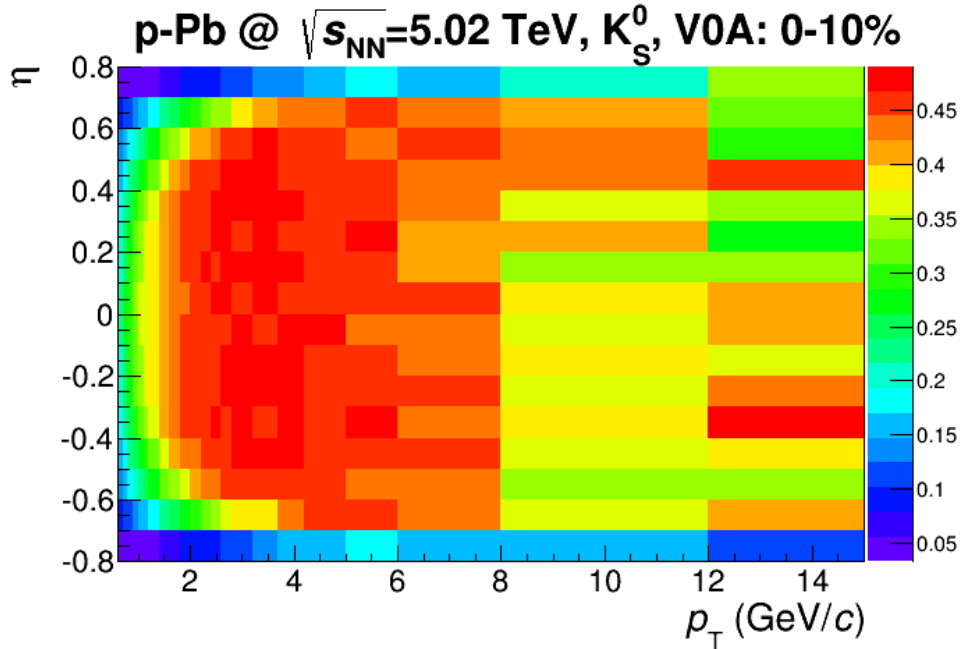


**Fig. 33:** 2D efficiency of inclusive  $V^0$ s as a function of  $p_T$  and  $\eta$ .

It has been shown that, for the single V<sup>0</sup>s, its efficiencies inside and outside the jets are same [10]. The difference between the efficiency of V<sup>0</sup>s in jets and inclusive V<sup>0</sup>s is caused by the bias of the jet  $\eta$  distribution. Figure 32 shows the normalized  $\eta$  distribution of JC  $K_S^0$  candidates (left) and OC  $K_S^0$  candidates with  $\Delta R_{\text{cut}} > 0.6$  (right) in  $0.6 < p_T < 1 \text{ GeV}/c$  in data. The results are compared to the  $\eta$  distribution of inclusive and  $K_S^0$  candidates. The  $\eta$  shape of JC  $K_S^0$  candidates is modified by the  $\eta$  distribution of the jets.

As shown in figure 33, the efficiency of inclusive V<sup>0</sup>s is non-uniform in  $\eta$ . The integrated  $p_{\text{T}}$ -dependent V<sup>0</sup> efficiency can be treated as weighted mean of the efficiency in the fine  $\eta$  bins:

$$\varepsilon(p_{\text{T}}) = \frac{\sum_{p_{\text{T}}} r(p_{\text{T}}, \eta)}{\sum_{p_{\text{T}}} g(p_{\text{T}}, \eta)} = \sum_{p_{\text{T}}} w(p_{\text{T}}, \eta) \varepsilon(p_{\text{T}}, \eta), \quad (10)$$

where:

- $r(p_{\text{T}}, \eta)$  and  $g(p_{\text{T}}, \eta)$  are the number of reconstructed and generated particles in each fine  $p_{\text{T}} - \eta$  bin, respectively;
- $w(p_{\text{T}}, \eta) = g(p_{\text{T}}, \eta) / \sum_{p_{\text{T}}} g(p_{\text{T}}, \eta)$  is the weight in the fine  $p_{\text{T}} - \eta$  bins;
- $\varepsilon(p_{\text{T}}, \eta) = r(p_{\text{T}}, \eta) / g(p_{\text{T}}, \eta)$  is the efficiency in the fine  $p_{\text{T}} - \eta$  bins.

According to eq. (10), the bin has the larger counts will contribute the higher weight in the integrated efficiency. As show in the left panel of figure 32, the bin towards to  $\eta = 0$  in JC V<sup>0</sup>  $\eta$  distribution has the larger contribution in the integrated efficiency than that in the  $\eta$  distribution of inclusive V<sup>0</sup>s. Due to the differential efficiency of V<sup>0</sup>s in the fine  $\eta$  bin towards to  $\eta = 0$  is higher than other, it makes the increasing of the JC V<sup>0</sup> efficiency w. r. t. that of the inclusive V<sup>0</sup>s in the low  $p_{\text{T}}$  as shown in figure 31.

To define the efficiency of the JC and OC V<sup>0</sup>s more precisely, a scaling approach based on choosing a reference fine  $\eta$  bin in data is proposed [11]. In this approach, the efficiency of JC and OC V<sup>0</sup>s in data is calculated as:

$$\varepsilon_{\text{RD}}(p_{\text{T}}) = \frac{\sum_{\eta} n(p_{\text{T}}, \eta)}{\sum_{\eta} n(p_{\text{T}}, \eta) / \varepsilon_{\text{MC}}(p_{\text{T}}, \eta)}, \quad (11)$$

where,  $n(p_{\text{T}}, \eta)$  is the number of reconstructed V<sup>0</sup>s in the give  $p_{\text{T}} - \eta$  bin in data and  $/\varepsilon_{\text{MC}}(p_{\text{T}}, \eta)$  is the 2D efficiency of inclusive V<sup>0</sup>s obtained in MC. The basic consideration for this formula is according to the efficiency of single V<sup>0</sup>s (either inside jets or outside jets) are the same and it is described by the efficiency of the inclusive V<sup>0</sup>s in the fine  $p_{\text{T}} - \eta$  bins in MC. The numerator are the reconstructed number of V<sup>0</sup>s in data, while the denominator corresponds to the number of generated V<sup>0</sup>s in data. In this case, the formula eq. (11) can not only be used to calculate the efficiency of the JC and OC V<sup>0</sup>s but also be used to correct the efficiency of inclusive V<sup>0</sup>s as well as the efficiency of NJ V<sup>0</sup>s.

As discussed in section 3.3 and section 5.2.1, the interpolated bin counting fit results in data and MC have to be subtracted in the term of  $n(p_{\text{T}}, \eta)$  and the numerator in the term of  $\varepsilon_{\text{MC}}(p_{\text{T}}, \eta)$  in eq. (11), respectively. But due to the restriction of the statistics, is it hard to make the stable bin counting fit in the side bands in the fine  $p_{\text{T}} - \eta$  bins in both data and MC. In the implementation, we assume the bin counting ratio  $R_{\text{Cbin}}$ , which defined in eq. (2), is independent on  $\eta$  in both data and MC (the uncertainty introduced by this assumption will be discussed in section 6.2.1). And the efficiency calculation in this analysis is modified as:

$$\varepsilon_{\text{RD}}(p_{\text{T}}) = \frac{f_{\text{Cbin}}^{\text{MC}}(p_{\text{T}}) \cdot \sum_{\eta} n(p_{\text{T}}, \eta)}{\sum_{\eta} n(p_{\text{T}}, \eta) / \varepsilon_{\text{MC}}(p_{\text{T}}, \eta)}, \quad (12)$$

where  $f_{\text{Cbin}}^{\text{MC}}(p_{\text{T}}) = R_{\text{Cbin}}^{\text{MC}}(p_{\text{T}}) / (1 + R_{\text{Cbin}}^{\text{MC}}(p_{\text{T}}))$ ,  $R_{\text{Cbin}}^{\text{MC}}(p_{\text{T}})$  is the  $p_{\text{T}}$ -dependent bin counting ratio in MC as show in the right panel of figure 4. Then in eq. (12) the term of  $n(p_{\text{T}}, \eta)$  and the numerator in the term of  $\varepsilon_{\text{MC}}(p_{\text{T}}, \eta)$  now correspond to the number of V<sup>0</sup> candidates (without the bin counting subtraction) in each fine  $p_{\text{T}} - \eta$  bin.

Figure 34 shows the ratio of the inclusive V<sup>0</sup> efficiency calculated by the scaling approach according to eq. (12) and the efficiency of inclusive V<sup>0</sup>s in MC which is shown in figure 30 in three event centrality bins. In general, the discrepancy between the efficiency calculated by this two approaches is  $\sim 1\%$ . The ratio of the efficiency of the JC, OC and NJ V<sup>0</sup>s calculated by the scaling approaching and those

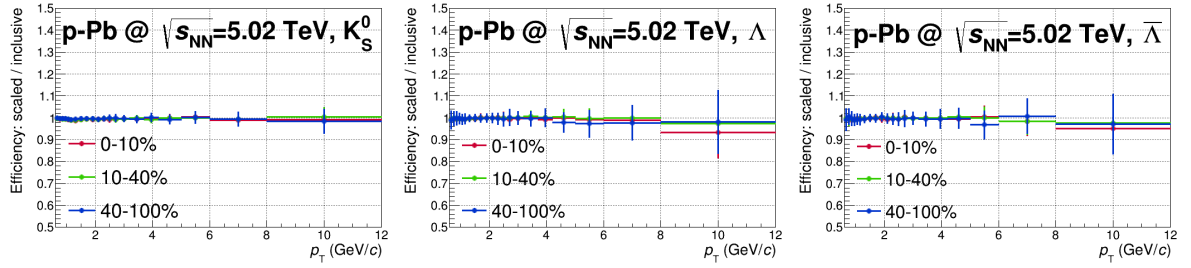


**Fig. 34:** The ratio between the scaled inclusive  $V^0$  efficiency calculated by using eq. (12) and the inclusive  $V^0$  efficiency in MC as shown in figure 30.

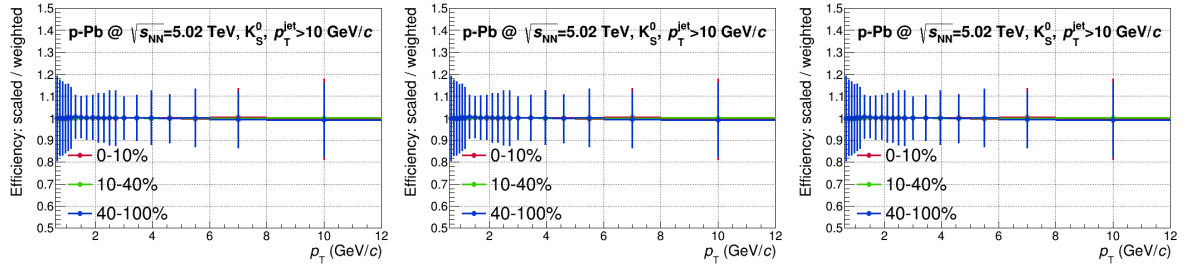


**Fig. 35:** The ratio between the scaled JC  $V^0$  efficiency calculated by using eq. (12) and the JC  $V^0$  efficiency calculated by the weighting approach described in appendix A. The results are obtained in  $p_T^{\text{jet}} > 10 \text{ GeV}/c$ .

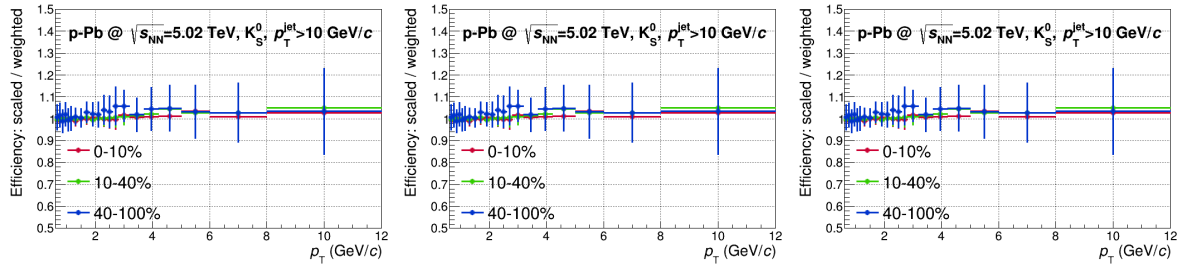


**Fig. 36:** The ratio between the scaled OC  $V^0$  efficiency calculated by using eq. (12) and the OC  $V^0$  efficiency calculated by the weighting approach described in appendix A. The results are obtained in  $p_T^{\text{jet}} > 10 \text{ GeV}/c$ . The OC  $V^0$ s are obtained with  $\Delta R_{\text{cut}} = 0.6$ .

calculated by a weighting approach (introduced in appendix A) are shown in figure 35, figure 36 and figure 37, respectively. The maximum deviation between the efficiencies obtained by these two methods is  $\sim 5\%$ .

Please note that, the error bars on the ratios in the figures are the statistic uncertainty propagated by ROOT. And indeed, the uncertainty propagation in the efficiency calculation is not straight forward. The details for the uncertainty will be discussed in section 6.1.

### 5.3 Underlying background subtraction

The corrected spectrum of any type of  $V^0$ s is given by:

$$\frac{dN}{dp_T} = m(p_T)/\varepsilon_{\text{RD}}(p_T), \quad (13)$$

where  $m(p_T)$  is number of  $V^0$ s in the given  $p_T$  bin after the bin counting subtraction,  $\varepsilon_{\text{RD}}(p_T)$  is the corrected  $V^0$  efficiency by the scaling procedure in eq. (12).

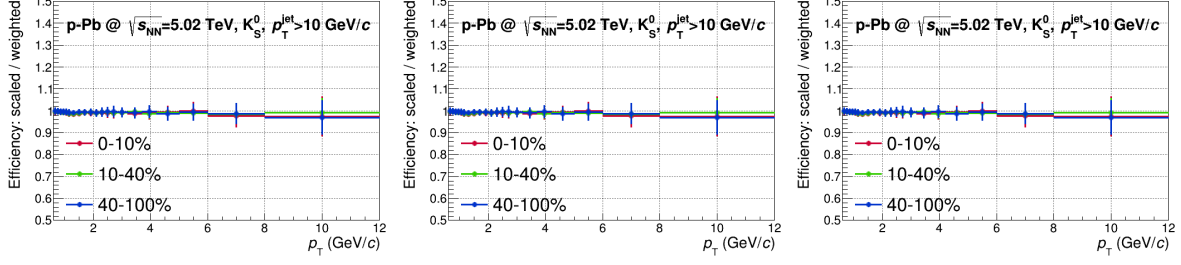


**Fig. 37:** The ratio between the scaled NJ  $V^0$  efficiency calculated by using eq. (12) and the NJ  $V^0$  efficiency calculated by the weighting approach described in appendix A.

Since the UE  $V^0$ s are used to estimate the UE background per acceptance area density inside the jet cone, to obtain the  $V^0$ s produced in jets (**JE**  $V^0$ s), we normalize the yields of both JC and UE  $V^0$ s to the per-event acceptance area unit to subtract the UE  $V^0$  background:

$$\frac{dM_{\text{JE}}}{dp_T} = \frac{dM_{\text{JC}}}{dp_T} - \frac{dM_{\text{UE}}}{dp_T}, \quad (14)$$

where, for the JC and UE  $V^0$ s the term  $dM/dp_T$  is given by:

$$\frac{dM_{\text{JC}/\text{UE}}}{dp_T} = \frac{1}{N_{\text{JC}/\text{UE}}^{\text{ev}}} \times \frac{1}{\Delta\eta \Delta\phi} \times \frac{dN_{\text{JC}/\text{UE}}}{dp_T}. \quad (15)$$

In eq. (15), the term  $dN_{\text{JC}/\text{UE}}/dp_T$  is the corrected JC or UE  $V^0$  spectrum defined in eq. (13),  $N_{\text{JC}/\text{UE}}^{\text{ev}}$  is the corresponding number of JC or UE events and  $\Delta\eta \times \Delta\phi$  is the per-event acceptance area for the JC or UE  $V^0$ s.

For the JC or OC  $V^0$ s, since they are obtained in the events have at least one selected jet in  $p_T^{\text{jet}} > p_T^{\min}$ <sup>5</sup>, the  $N_{\text{JC}/\text{OC}}^{\text{ev}}$  for the JC or OC  $V^0$ s is number of events with at least one selected jet in  $p_T^{\text{jet}} > p_T^{\min}$ . For NJ  $V^0$ s, the  $N_{\text{NJ}}^{\text{ev}}$  is the number of events have no jet in  $p_T > 5 \text{ GeV}/c$ .

According to the definition, the per-event acceptance area for NJ  $V^0$ s is equal to the acceptance of the inclusive  $V^0$  define in section 5.1.1:

$$[\Delta\eta \times \Delta\phi]_{\text{NJ}} = 2 \times 0.75 \times 2\pi. \quad (16)$$

Concerning the calculation of the per-event acceptance area for the JC or OC  $V^0$ s ( $[\Delta\eta \times \Delta\phi]_{\text{JC}/\text{OC}}$ ), the following MC approach is adopted:

1. generate the a given number of testing particles with the randomized  $\eta$  and  $\phi$  in the  $V^0$  acceptance according to the  $\eta - \phi$  distribution of the the JC or OC  $V^0$  candidates (in this analysis,  $10^3$  testing particles are generated in each event),
2. match the testing particles to the jets in each given event and count the numbers of the testing particles inside and outside the jet cones;
3. the ratio of the number of the JC/OC particles and the number of total generated particles gives the fraction of acceptance for the JC/OC  $V^0$ s in the given event;
4. the final acceptance correction factor of JC/OC  $V^0$ s is given by the average of the event-by-event acceptance fraction.

<sup>5</sup>As discussed in section 5.1.3, there are two set of values are chosen for the  $p_T^{\min}$ :  $p_T^{\min} = 10 \text{ GeV}/c$  and  $p_T^{\min} = 20 \text{ GeV}/c$  in this analysis.

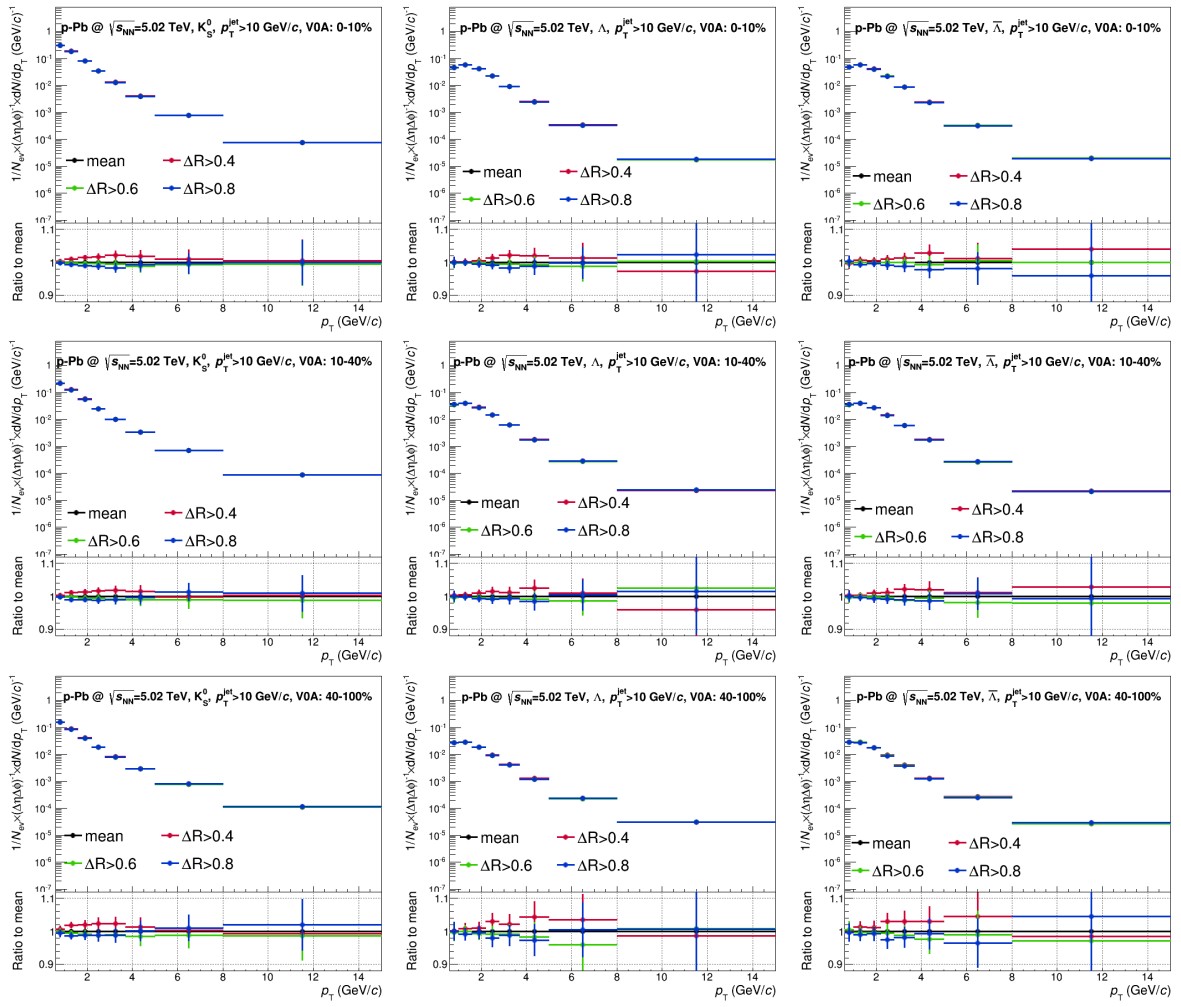


Fig. 38: Normalized OC V<sup>0</sup>s with different  $\Delta R$  in  $p_T^{\text{jet}} > 10 \text{ GeV}/c$ .

#### 5.4 Feeddown subtraction

To obtain the final corrected spectra for  $\Lambda$  and  $\bar{\Lambda}$  the feeddown components from  $\Xi$  decays has to be subtracted. The method used for the feeddown subtraction for the inclusive V<sup>0</sup>s is introduced in [1]. According to this method, the subtraction has to be applied before the efficiency correction.

To apply the feeddown subtraction of the V<sup>0</sup>s in jets, the following issues has to be considered:

- we have not measured the  $\Xi$  produce inside jets yet;
- the V<sup>0</sup>s produced inside jets are obtained by subtract the UE V<sup>0</sup>s from the JC V<sup>0</sup>s and the JC V<sup>0</sup>s are composed by the following four components:

$$\text{JC} = \text{JC}_H + \text{JC}_F + \text{UE}_H + \text{UE}_F, \quad (17)$$

where,

- $\text{JC}_H$  V<sup>0</sup>s is the primary V<sup>0</sup>s produced inside jets and they are what we are going to measured in this analysis;
- $\text{JC}_F$  V<sup>0</sup>s is the feeddown V<sup>0</sup>s matched with the jets;
- $\text{UE}_H$  V<sup>0</sup>s is the primary V<sup>0</sup>s in matched with the jets but from the underlying event;

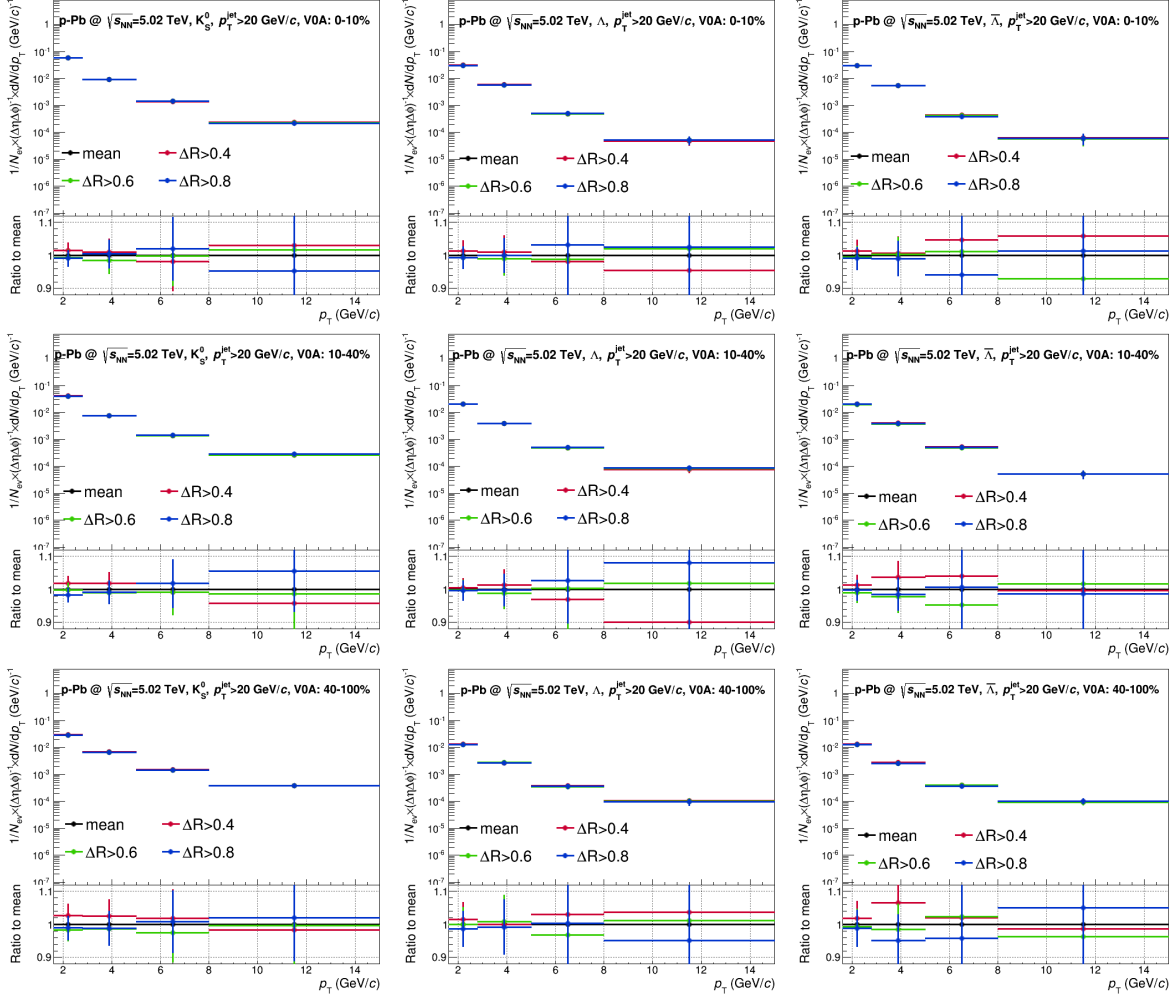


**Fig. 39:** Normalized OC  $V^0$ s with different  $\Delta R$  in  $p_T^{\text{jet}} > 20 \text{ GeV}/c$ .

–  $\text{UE}_F$  is the feeddown  $V^0$ s matched with jets but from the underlying event.

Since the efficiency correction will not change the ratios of  $\text{JC}_H$   $V^0$ s/ $\text{JC}_F$   $V^0$ s and  $\text{UE}_H$   $V^0$ s/ $\text{UE}_F$   $V^0$ s in the  $\text{JC}$   $V^0$  component, the following steps are used to subtract the feeddown contributions for the  $V^0$  produced inside jets:

1. apply the efficiency correction for both  $\text{JC}$  and  $\text{UE}$   $V^0$ s without the feeddown subtraction;
2. subtract the normalized  $\text{UE}$  component from the  $\text{JC}$   $V^0$ s, in this procedure, the last two terms in eq. 17 are subtracted;
3. subtract the feeddown  $V^0$ s matched with jets ( $\text{JC}_F$   $V^0$ s) according to the estimated feeddown fraction.

The uncertainty of this feeddown subtraction strategy will be discussed in section 6.2.3.

## 5.5 Normalized results

The normalized spectra of OC  $V^0$ s are shown in figure 38 and figure 39 with  $p_T^{\text{jet}} > 10 \text{ GeV}/c$  and  $p_T^{\text{jet}} > 20 \text{ GeV}/c$ , respectively. The charged jets are reconstructed with  $R_{\text{jet}} = 0.4$ . In general, the difference between the OC  $V^0$ s with different  $\Delta R_{\text{cut}}$  is small ( $\sim 2\%$ ). With smaller  $\Delta R_{\text{cut}}$  (e.g.  $\Delta R_{\text{cut}} = 0.4$ ),

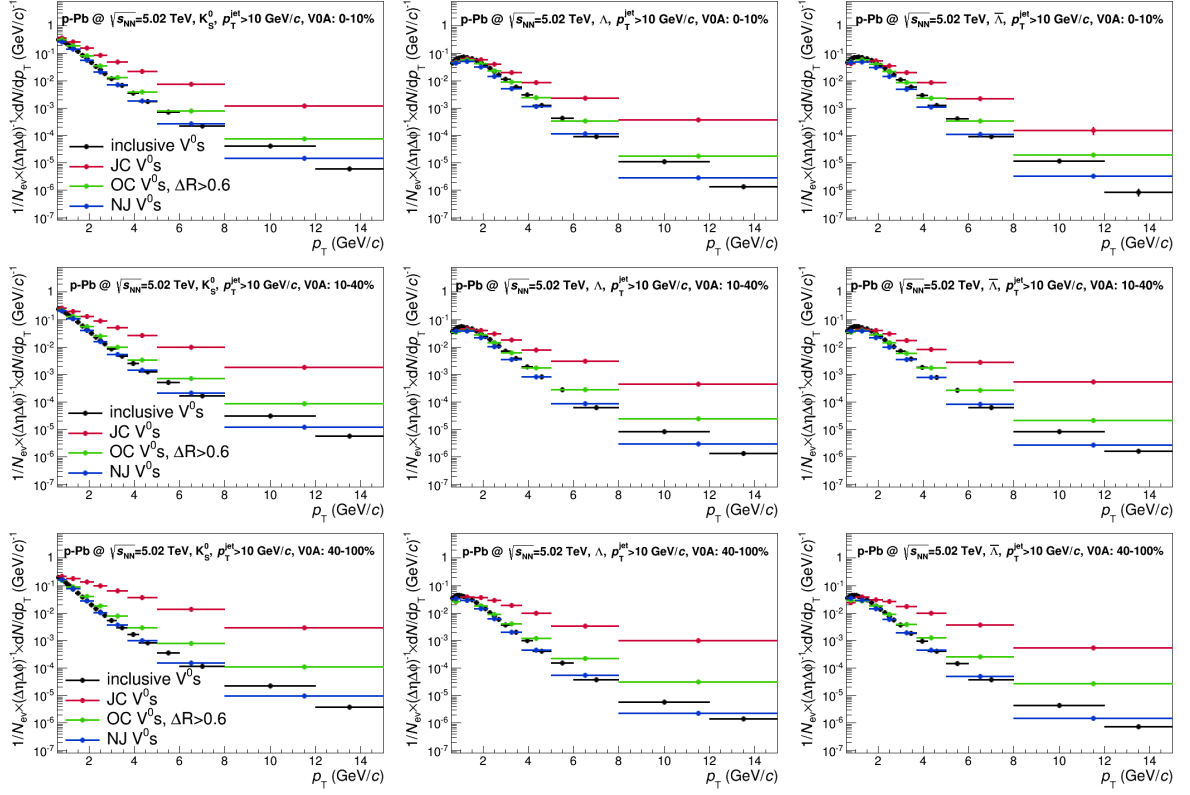


**Fig. 40:** Normalized JC V<sup>0</sup>s and UE V<sup>0</sup>s in  $p_T^{\text{jet}} > 10 \text{ GeV}/c$ , results are compared to the inclusive V<sup>0</sup>s.

the correlations between the OC component and JC V<sup>0</sup>s is stronger. And its normalized spectrum is systematically higher than the ones with larger  $\Delta R_{\text{cut}}$ .

The normalized  $p_T$  spectra for different type of V<sup>0</sup>s are compared in figure 40 and figure 41 with  $p_T^{\text{jet}} > 10 \text{ GeV}/c$  and  $p_T^{\text{jet}} > 20 \text{ GeV}/c$ , respectively. As expected, the spectra of OC and NJ V<sup>0</sup>s are very close to the that of the inclusive V<sup>0</sup>s in the low  $p_T$  region since the inclusive V<sup>0</sup> production is dominated by the V<sup>0</sup>s from the underlying events. In the high  $p_T$  region, the spectra of OC V<sup>0</sup>s is harder than that of the inclusive V<sup>0</sup>s and the spectra of NJ V<sup>0</sup>s is softer than the inclusive ones. As mentioned in section 5.1.3 the OC V<sup>0</sup>s may include the component come from the jets excluded by the jet selection. And the contribution from the V<sup>0</sup>s produced inside the jets are highly suppressed in the sample of the NJ V<sup>0</sup>s and it makes its spectrum is softer than that of the inclusive V<sup>0</sup>s. Despite this difference, the spectra of both the OC and NJ V<sup>0</sup>s are much softer than that of the JC V<sup>0</sup>s (as expected, the high  $p_T$  V<sup>0</sup> are mainly contributed by the jet production), the uncertainty introduced by the UE V<sup>0</sup> subtraction should be small in the high  $p_T$  region.

## 6 Uncertainty

### 6.1 Statistic uncertainty

The eq. (15) gives the normalized the  $p_T$  spectrum for any type of V<sup>0</sup>s. To propagate the statistics uncertainty in this formula, we have to write it in a more explicitly way and study the correlations

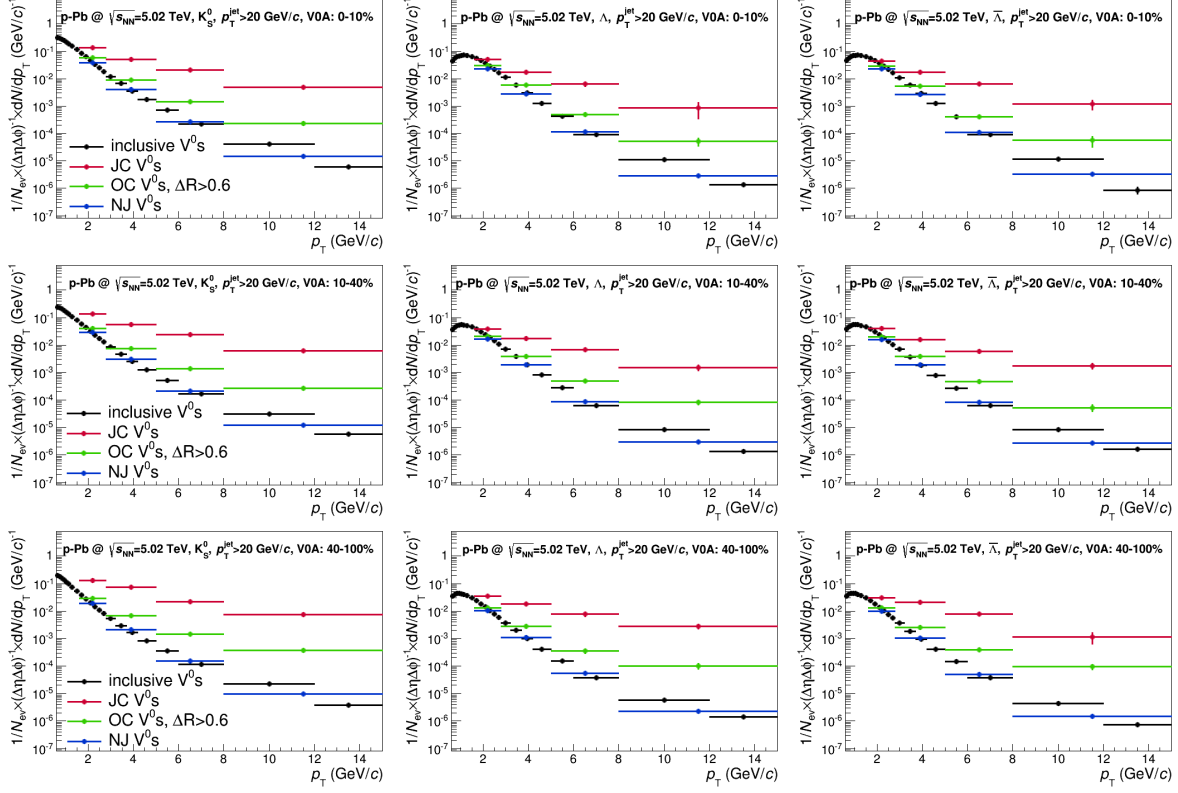


**Fig. 41:** Normalized JC  $V^0$ s and UE  $V^0$ s in  $p_T^{\text{jet}} > 20 \text{ GeV}/c$ , results are compared to the inclusive  $V^0$ s.

between the terms in it:

$$\begin{aligned}
 M(p_T) &= \frac{dM}{dp_T} = \frac{1}{N^{\text{ev}}} \times \frac{1}{\Delta\eta\Delta\phi} \times \frac{dN}{dp_T} \\
 &= \frac{1}{N^{\text{ev}}} \times \frac{1}{\Delta\eta\Delta\phi} \times m(p_T)/\varepsilon_{\text{RD}}(p_T) \\
 &= \frac{1}{N^{\text{ev}}} \times \frac{1}{\Delta\eta\Delta\phi} \times m(p_T)/f_{\text{Cbin}}^{\text{MC}}(p_T) \times \sum_{\eta} w_{\text{RD}}(p_T, \eta)/\varepsilon_{\text{MC}}(p_T, \eta)
 \end{aligned} \tag{18}$$

where,

$$w_{\text{RD}}(p_T, \eta) = n(p_T, \eta)/\sum_{\eta} n(p_T, \eta). \tag{19}$$

In eq. (15) the term  $1/N^{\text{ev}} \times 1/\Delta\eta\Delta\phi$  is the normalization factor of the spectrum, we do not consider its statistic uncertainty. In the rest of terms,  $m(p_T)$  is corrected with  $w_{\text{RD}}(p_T, \eta)$  and  $f_{\text{Cbin}}^{\text{MC}}$  is corrected with  $\varepsilon_{\text{MC}}(p_T, \eta)$ . Indeed, the term  $\sum_{\eta} w_{\text{RD}}(p_T, \eta)/\varepsilon_{\text{MC}}(p_T, \eta)$  has the role as the inverse of the  $\eta$ -integrated efficiency in data and treat it independent to the  $m(p_T)$  and  $f_{\text{Cbin}}^{\text{MC}}(p_T)$ . Under this approximation, the statistic uncertainty of  $M(p_T)$  is given by:

$$\left[ \frac{\sigma_M(p_T)}{M(p_T)} \right]^2 = \left[ \frac{\sigma_m(p_T)}{m(p_T)} \right]^2 + \left[ \frac{\sigma_{f_{\text{Cbin}}^{\text{MC}}}(p_T)}{f_{\text{Cbin}}^{\text{MC}}(p_T)} \right]^2 + \left[ \frac{\sigma_{\varepsilon_{\text{scl}}}(p_T)}{\varepsilon_{\text{scl}}(p_T)} \right]^2, \tag{20}$$

where:  $1/\varepsilon_{\text{scl}}(p_T) = \sum_{\eta} w_{\text{RD}}(p_T, \eta)/\varepsilon_{\text{MC}}(p_T, \eta)$ .

$m_{p_T}$  is the number of  $V^0$ s in the signal window after subtracting the interpolated results from the bin counting fit in data, its statistic uncertainty is given by:

$$\sigma_m^2(p_T) = n(p_T) + c(p_T), \tag{21}$$

where  $n(p_T) = \sum_\eta n(p_T, \eta)$  is the selected number of V<sup>0</sup> candidates in the signal window,  $c(p_T)$  is the integrated bin counting fit results in the signal window.

$f_{\text{Cbin}}^{\text{MC}}(p_T)$  is defined in eq. (12):

$$f_{\text{Cbin}}^{\text{MC}}(p_T) = a(p_T)/r(p_T), \quad (22)$$

where the definition of  $r(p_T)$  ( $a(p_T)$ ) is the same as  $n(p_T)$  ( $c(p_T)$ ) in eq. (21) just  $r(p_T)$  ( $a(p_T)$ ) is obtained in MC and  $n(p_T)$  ( $c(p_T)$ ) is obtained in data. In eq. (22), the independent variables are  $a(p_T)$  and  $r(p_T) - a(p_T)$ , the statistic uncertainty of  $f_{\text{Cbin}}^{\text{MC}}(p_T)$  is given by:

$$\sigma_{f_{\text{Cbin}}^{\text{MC}}}^2(p_T) = f_{\text{Cbin}}^{\text{MC}}(p_T)[1 - f_{\text{Cbin}}^{\text{MC}}(p_T)]/r(p_T). \quad (23)$$

The statistic uncertainty of  $\varepsilon_{\text{scl}}(p_T)$  is given by:

$$[\frac{\sigma_{\varepsilon_{\text{scl}}}(p_T)}{\varepsilon_{\text{scl}}(p_T)}]^2 = \sum_\eta \{ [\frac{\sigma_{w_{\text{RD}}}(p_T, \eta)}{w_{\text{RD}}(p_T, \eta)}]^2 + [\frac{\sigma_{\varepsilon_{\text{MC}}}(p_T, \eta)}{\varepsilon_{\text{MC}}(p_T, \eta)}]^2 \}. \quad (24)$$

According to the definition,

$$w_{\text{RD}}(p_T, \eta) = \frac{n(p_T, \eta)}{n(p_T)} = \frac{n(p_T, \eta)}{n(p_T, \eta) + \sum_{\eta' \neq \eta} n(p_T, \eta')}. \quad (25)$$

Since the  $n(p_T, \eta)$  is uncorrelated to  $\sum_{\eta' \neq \eta} n(p_T, \eta')$ , the statistic uncertainty of  $w_{\text{RD}}(p_T, \eta)$  is:

$$\sigma_{w_{\text{RD}}}^2(p_T, \eta) = w(p_T, \eta)[1 - w_{\text{RD}}(p_T, \eta)]/n(p_T). \quad (26)$$

The  $\varepsilon_{\text{MC}}(p_T, \eta)$  is the efficiency of the V<sup>0</sup>s uncorrected by the interpolated bin counting fit result. In this analysis, the V<sup>0</sup>s ( $K_S^0$ ,  $\Lambda$  and  $\bar{\Lambda}$ ) are reconstructed by the decay channels:

$$K_S^0 \rightarrow \pi^+ \pi^-, \quad \Lambda \rightarrow p \pi^-, \quad \text{and} \quad \bar{\Lambda} \rightarrow \bar{p} \pi^+,$$

the corresponding branching ratio is also considered in the efficiency  $\varepsilon_{\text{MC}}(p_T, \eta)$  and the statistic uncertainty of  $\varepsilon_{\text{MC}}(p_T, \eta)$  is:

$$\sigma_{\varepsilon_{\text{MC}}}^2(p_T, \eta) = \varepsilon_{\text{MC}}(p_T, \eta)[r_b - \varepsilon_{\text{MC}}(p_T, \eta)]/g(p_T, \eta)/r_b, \quad (27)$$

where  $g(p_T, \eta)$  is the number of generated particles which is used to build the denominator of the efficiency and  $r_b$  is the branching ratio for the corresponding decay channel.

At final, the statistic uncertainty of the V<sup>0</sup> spectra is given by taking all the components into eq. (20). Since the samples of JC and UE V<sup>0</sup>s are independent on each other, the statistic uncertainty propagation for the V<sup>0</sup>s produced inside jets (JE V<sup>0</sup>s) is straightforward:

$$\sigma_{M_{\text{JE}}}^2(p_T) = \sigma_{M_{\text{JC}}}^2(p_T) + \sigma_{M_{\text{UE}}}^2(p_T), \quad (28)$$

where the  $\sigma_{M_{\text{JC/UE}}}^2(p_T)$  is calculated according to eq. (20). The general concepts about the statistic uncertainty calculations in this section are discussed in appendix B.

## 6.2 Systematic uncertainty

The systematic uncertainty of the JC and UE V<sup>0</sup>s in this analysis contains the following sources:

- uncertainty on single V<sup>0</sup> analysis;
- uncertainty on underlying V<sup>0</sup> subtraction;
- uncertainty on feeddown correction;
- uncertainty on jet  $p_T$  scale.

| selection                                                     | very loose | loose   | tight   | very tight |
|---------------------------------------------------------------|------------|---------|---------|------------|
| $V^0$ 2D decay radius (cm)                                    | > 0.3      | > 0.4   | > 0.6   | > 0.7      |
| negative track DCA to PV (cm)                                 | > 0.050    | > 0.055 | > 0.070 | > 0.080    |
| positive track DCA to PV (cm)                                 | > 0.050    | > 0.055 | > 0.070 | > 0.080    |
| DCA between $V^0$ daughters ( $\sigma$ )                      | < 1.50     | < 1.25  | < 0.75  | < 0.50     |
| $\cos \theta_{\text{pointing}}$ for $K_S^0$                   | > 0.95     | > 0.96  | > 0.98  | > 0.99     |
| $\cos \theta_{\text{pointing}}$ for $\Lambda (\bar{\Lambda})$ | > 0.993    | > 0.994 | > 0.996 | > 0.997    |

**Table 5:**  $V^0$ s topological selection criteria used for the systematic uncertainty estimation.

| selection                                      | $K_S^0$             | $\Lambda (\bar{\Lambda})$ |
|------------------------------------------------|---------------------|---------------------------|
| proper life time $mL/p$ (cm)                   | < 12, < 30 and < 40 | < 20 and < 40             |
| competing $V^0$ rejection ( $\text{MeV}/c^2$ ) | > 3 and > 6         | without cut               |
| TPC $dE/dx$ selection ( $\sigma$ )             | without cut         | < 4, < 6 and < 7          |

**Table 6:** Selection criteria of  $V^0$  proper lifetime, competing mass and TPC  $dE/dx$  for the systematic uncertainty estimation.

| selection                                    | cut value     |
|----------------------------------------------|---------------|
| number of crossed rows in TPC                | > 75 and > 80 |
| number of crossed rows/ findable rows in TPC | > 0.95        |

**Table 7:** Values of cuts on TPC rows for the  $V^0$  selection.

### 6.2.1 Uncertainty on single $V^0$ analysis

The strategy of systematic uncertainty estimation of single  $V^0$  analysis is summarized in [1]. It contains the following three sources:

- systematic uncertainty on  $V^0$  candidate selection;
- systematic uncertainty on  $V^0$  signal extraction;
- systematic uncertainty on material budget.

The uncertainty on the material budget is estimated from previous checks in earlier analyses and it is estimated as 4% in both pp and p–Pb collisions.

**Systematic uncertainty on  $V^0$  candidate selection** The systematic uncertainty on  $V^0$  candidate selection is estimated by varying the following cuts one by one in both data and MC.

- Topological selection: it is estimated by varying the topological variables listed in table 3 with four additional different values as summarized in table 5;
- selections of proper lifetime, competing mass and TPC  $dE/dx$  for  $V^0$  daughter identification: the varied cut values for  $K_S^0$  and  $\Lambda (\bar{\Lambda})$  are listed in table 6;
- selection of the crossed TPC rows for  $V^0$  daughters: it contains two set of cuts, the number of crossed TPC rows and the ratio between the number of crossed TPC row and the number of finable rows in TPC, the cut values are listed in table 7.

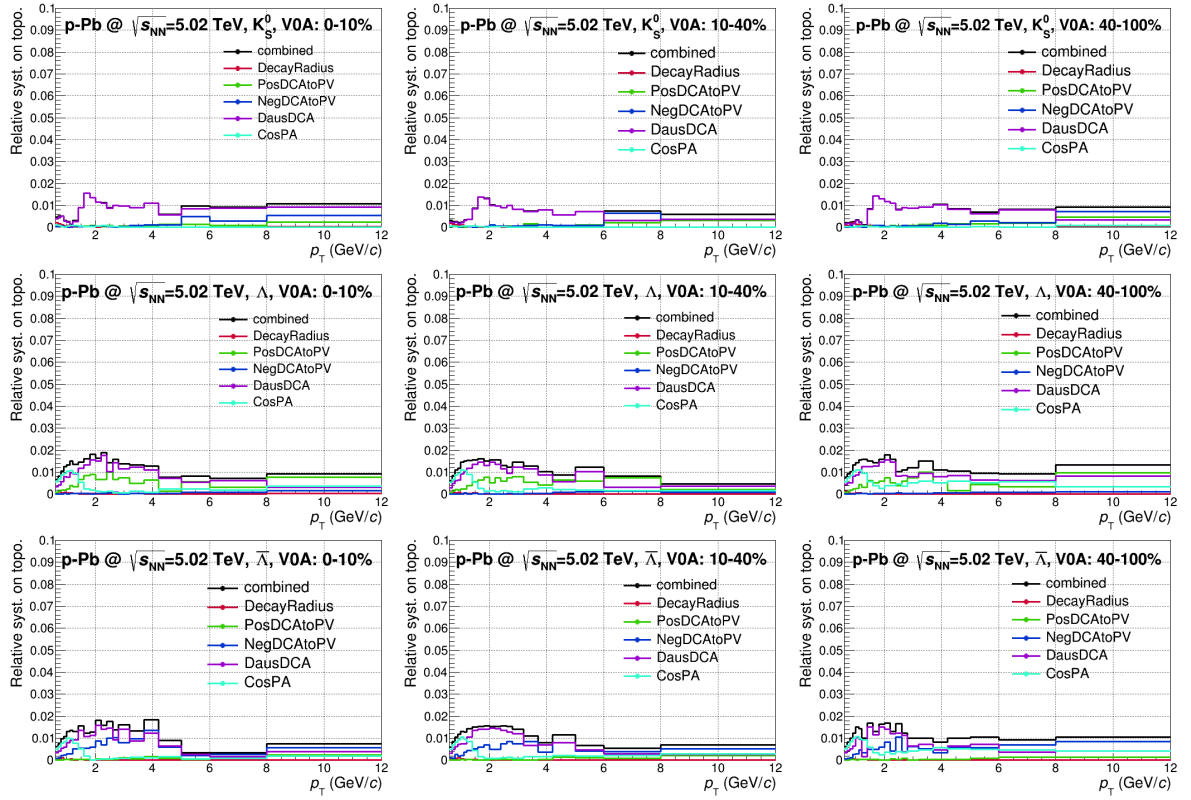


**Fig. 42:** Systematic uncertainty on topological selection as a function of  $p_T$  in three event multiplicity bins with the V0A centrality estimator.

For each of the cut, the uncertainty is estimated by the maximum deviation between the results with the varied cuts and that with the default cut (listed in section 3.2). The final uncertainty is given by quantitative sum of all the uncertainty sources.

**Systematic uncertainty on V<sup>0</sup> signal extraction** As mentioned in section 3.3, the number of V<sup>0</sup> signals is extracted in the window defined in  $N\sigma$  after subtracting the interpolated bin counting fit result. The default value to build the signal window is  $N = 5$ . The uncertainty on V<sup>0</sup> signal extraction is given by  $N = 4, 6$  and  $7$ . The value of  $N$  is also changed simultaneously in both data and MC. The systematic uncertainty is estimated as the maximum deviation between the results with varied  $N$  values and that with  $N = 5$ .

**Relative uncertainty of inclusive V<sup>0</sup>s** Figures 42 shows the uncertainty on topological selection for different variables. The results are shown as a function of  $p_T$  and in three event multiplicity bins with the V0A centrality estimator. The combined results are the quantitative sum of all the sources. In general, the uncertainty on the topological selection varies from 2% to 1% from low to high  $p_T$ . For both  $K_S^0$  and  $\Lambda(\bar{\Lambda})$  the uncertainty is dominated by the uncertainty on the DCA between the daughter tracks. But the contribution from the uncertainty on  $\cos \theta_{\text{pointing}}$  becomes important in the hight  $p_T$  region for  $\Lambda(\bar{\Lambda})$ . The uncertainty on TPC rows selection are shown in figure 43. In all of the cases, the uncertainty on number of crossed TPC rows is small (< 1%). But the uncertainty on the ratio of number of crossed rows and findable rows in TPC is much larger. In general, it has the order of  $\mathcal{O}(2\%)$  and it achieves to 3% – 5% in some cases, especially in hight  $p_T$  region.

The systematical uncertainties on the V<sup>0</sup> candidates selection and V<sup>0</sup> signal extraction are compared in figure 44. The combined uncertainty is the quantitative sum of all the sources. For  $K_S^0$ , the combined

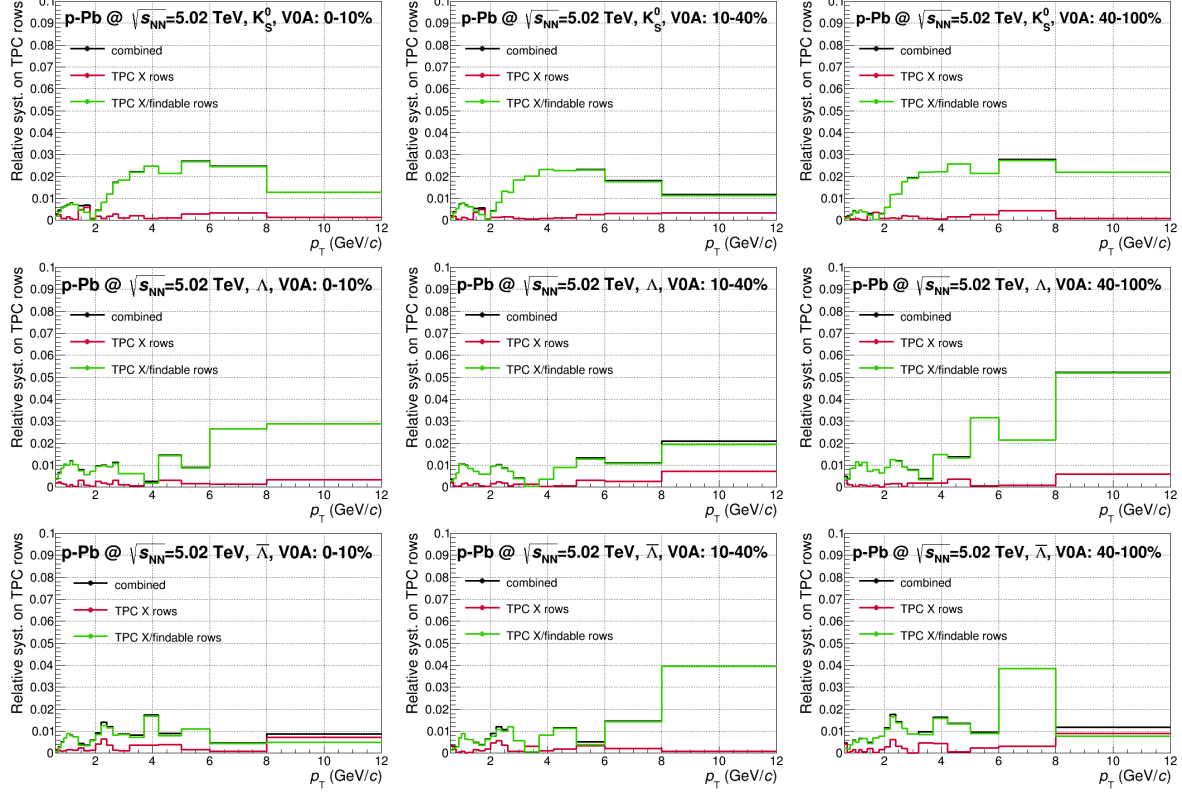


**Fig. 43:** Systematic uncertainty on TPC rows selection for the  $V^0$  daughter tracks. Results are shown as a function of  $p_T$  and in three event multiplicity bins with the V0A centrality estimator.

uncertainty is dominated by the uncertainty on signal extraction. And the contribution from the TPC rows selection becomes important in high  $p_T$  region. For  $\Lambda$  and  $\bar{\Lambda}$ , the combined uncertainty is mainly contributed by the uncertainty on proper lifetime selection in low  $p_T$  region, and in high  $p_T$  the uncertainty is dominated by the uncertainty on the competing mass selection since this cut has been removed to estimate the corresponding uncertainty for  $\Lambda$  and  $\bar{\Lambda}$ .

**Uncertainty of the JC and UE  $V^0$ s** The different uncertainty sources on the single  $V^0$  analysis of the inclusive  $V^0$ s are summarized in figure 44. Since the  $V^0$ s and jets are reconstructed independently in this analysis, the uncertainty on the  $V^0$  candidate selection and that on the material budget of the inclusive  $V^0$ s should be the same as those of the JC and UE  $V^0$ s. In particular, the statistics of the inclusive  $V^0$ s is much higher than the the JC or UE  $V^0$ s, the correlations between the systematic uncertainty on the  $V^0$  candidates selection estimated by using the inclusive  $V^0$ s and the statistics is week.

For the uncertainty on  $V^0$  single extraction, since it contains the uncertainty on the bin counting fit which depends on the statistics. In this case, we reproduced the procedures used to estimate the uncertainty on  $V^0$  signal extraction to the JC and UE  $V^0$ s. This uncertainty is estimated as 6% with  $p_T^{\text{jet}} > 10 \text{ GeV}/c$  and 10% with  $p_T^{\text{jet}} > 20 \text{ GeV}/c$  independent with the  $V^0$   $p_T$ .

**Discussion** In section 5.2.2, to obtain the  $\eta$  modified  $V^0$  efficiency (the eq. (12)), we assume that, the bin counting ratio (the  $R_{\text{Cbin}}$  defined in eq. (2)) in the integrated  $\eta$  region and in each sub- $\eta$  region is the same in both data and MC. Indeed, this ratio should be changed between the fine  $\eta$  bins due to the acceptance of the  $V^0$  daughter tracks (the bin counting ratio in the  $\eta$  region towards to the bound of the daughter track acceptance should be different from that in the rest ones). Here, we claim that, the uncertainty introduced by this assumption is included in the uncertainty on single  $V^0$  analysis, because

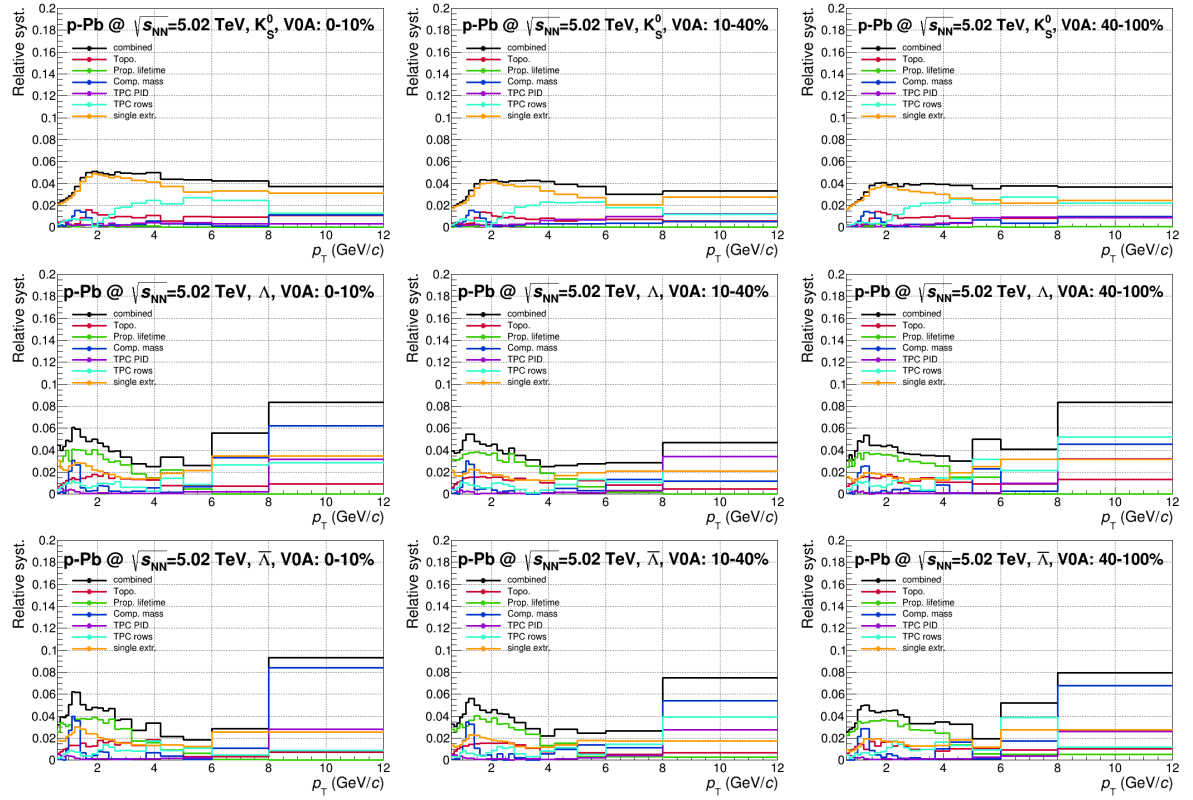


**Fig. 44:** Uncertainties on V<sup>0</sup>s candidates selection and V<sup>0</sup> signal extraction. The results are shown as a function of  $p_T$  and in three event multiplicity bins with the V0A centrality estimator. The combined uncertainty are the quantitative sum of all the sources.

of the following reasons:

- the contribution in the  $\eta$  region towards to the bound of the daughter track acceptance is small in the final result;
- the bin counting ratio will be changed if we varying the cuts of the V<sup>0</sup> daughter track selection and V<sup>0</sup> topological selection to estimate the uncertainty on V<sup>0</sup> candidate selection;
- when we varying the signal window and slide bands to the estimate the uncertainty on V<sup>0</sup> signal extraction, it also changes the bin counting ratio since the inputs for the bin counting fit have been changed.

In this case, the fluctuations of the bin counting ratio between the fine  $\eta$  bins will be contained in the uncertainty on the single V<sup>0</sup> analysis.

### 6.2.2 Uncertainty on underlying V<sup>0</sup> subtraction

As mentioned in section 5.1.3, the underlying V<sup>0</sup>s are estimated by two approached: the OC V<sup>0</sup>s and the NJ V<sup>0</sup>s. According to the discussion in section 5.5, the spectrum of OC V<sup>0</sup>s is harder than that of the NJ V<sup>0</sup>s. And for the OC V<sup>0</sup>s, the normalized spectrum built with the smaller  $\Delta R_{\text{cut}}$  is higher than those build with the larger  $\Delta R_{\text{cut}}$ . To estimate the uncertainty on underlying V<sup>0</sup> subtraction, we use the OC V<sup>0</sup>s with  $\Delta R_{\text{cut}} = 0.6$  to build the centre value of the spectrum for the V<sup>0</sup>s produced inside jet:

$$\text{JE} = \text{JC} - \text{OC}(\Delta R_{\text{cut}} = 0.6), \quad (29)$$

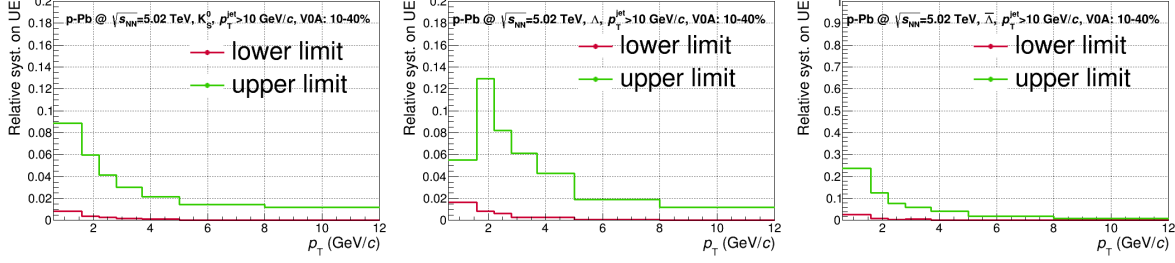


**Fig. 45:** The relative systematic uncertainty on underlying  $V^0$  subtraction. The results are shown in  $10 - 40\%$  event multiplicity bin. The upper and lower uncertainty bands are shown in green and red, respectively.

and use the OC  $V^0$ s with  $\Delta R_{\text{cut}} = 0.4$  and NJ  $V^0$ s to build the asymmetry band:

$$[\text{JC} - \text{OC}(\Delta R_{\text{cut}} = 0.4), \text{JC} - \text{NJ}]. \quad (30)$$

The band defined in eq. (30) gives region where the spectra of the  $V^0$ s produced inside the jets is located and it is not equal to the RMS which is generally used to define the uncertainty. By following the strategy in [12], we assume the distribution of JE  $V^0$ s is uniform<sup>6</sup> in the band defined in eq. (30), then the RMS of the band is given by:

$$\left[ \frac{\text{JC} - \text{OC}(\Delta R_{\text{cut}} = 0.4)}{\sqrt{12}}, \frac{\text{JC} - \text{NJ}}{\sqrt{12}} \right]. \quad (31)$$

The eq. (31) is used to give the uncertainty on the underlying  $V^0$  subtraction on the  $p_T$  spectrum. As an example, the relative systematic uncertainty on underlying  $V^0$  subtraction in  $10 - 40\%$  event multiplicity bin is presented in figure 45. The upper and lower bands in eq. (31) are shown in green and red, respectively. The lower limit of the uncertainty is always small. For the upper limit, it arises to  $\sim 10\%$  in low  $p_T$  region, then it decreases to a few percent in the high  $p_T$  region as expected. In principle, the uncertainty for  $\Lambda$  and  $\bar{\Lambda}$  should be very similar. But figure 45 shows a large difference of the upper limit of the uncertainty between  $\Lambda$  and  $\bar{\Lambda}$  in the low  $p_T$  region. This could be caused by the UE  $V^0$ s is dominated in the low  $p_T$  and the uncertainty on UE  $V^0$  subtraction is more sensitive to the statistic fluctuations than that in the high  $p_T$  region.

Since the OC and NJ  $V^0$ s are correlated with the jet  $p_T$  which used to define the OC and NJ events, to calculate the uncertainty on underlying  $V^0$  subtraction for the  $K_S^0$ -to- $\Lambda$  ratio we did not propagate them from the uncertainty on the  $V^0$  spectrum directly but use the following steps:

- calculate the  $K_S^0$ -to- $\Lambda$  ratio ( $R_{K/\Lambda}$ ) with varies UE  $V^0$ s;
- the centre value is given by using the OC  $V^0$ s with  $R_{\text{cut}} = 0.6$ :

$$R_{K/\Lambda}(\text{JC} - \text{OC}_{R_{\text{cut}}=0.6}); \quad (32)$$

- the upper and lower limits of the uncertainty are given by:

$$\left[ \frac{R_{K/\Lambda}(\text{JC} - \text{OC}_{R_{\text{cut}}=0.4})}{\sqrt{12}}, \frac{R_{K/\Lambda}(\text{JC} - \text{NJ})}{\sqrt{12}} \right]. \quad (33)$$

As an example, figure 46 shows one of uncertainty results for the  $K_S^0$ -to- $\Lambda$  ratio.

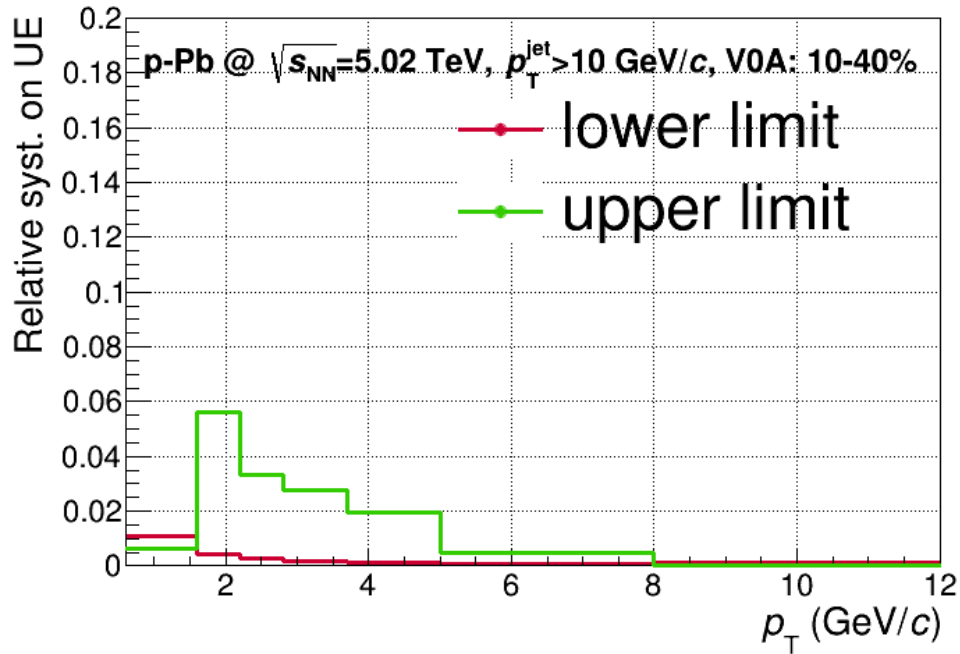


**Fig. 46:** The relative systematic uncertainty on underlying  $V^0$  subtraction for the  $K_S^0$ -to- $\Lambda$  ratio. The results are shown in 10 – 40% event multiplicity bin. The upper and lower uncertainty bands are shown in green and red, respectively.

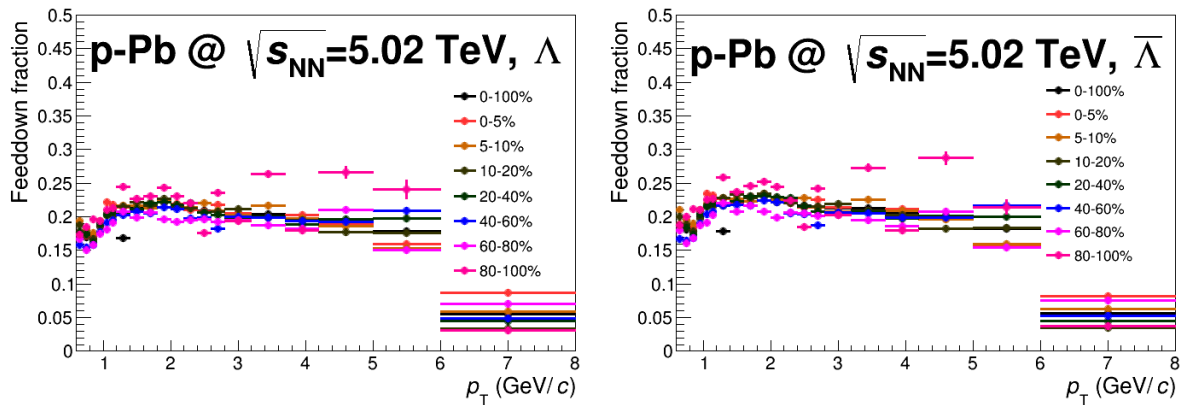


**Fig. 47:** Feeddown fraction of inclusive  $\Lambda$  (left) and  $\bar{\Lambda}$  (right) from  $\Xi$  decays obtained in data.

### 6.2.3 Uncertainty on feeddown subtraction

The uncertainty on feeddown subtraction (for  $\Lambda$  and  $\bar{\Lambda}$ ) in the inclusive  $V^0$  spectrum is from the uncertainty on  $\Xi$  measurement and the feeddown production extrapolation (in hight  $p_T$ ) [1, 2]. The value varies from 5% (in  $p_T < 3.7 \text{ GeV}/c$ ) to 7% (in  $p_T > 3.7 \text{ GeV}/c$ ) [2].

To correct the feeddown for the  $V^0$ s inside jets, one has to consider the production of  $\Xi$  inside jets could be different from that of the inclusive one. And it will make difference between the feeddown fraction of the inclusive  $V^0$ s and  $V^0$ s produced inside jets.

<sup>6</sup>As discussed in [12], the advantage to assume the uniform distribution in the band is that, it can minimize the bias introduced by the assumption of the distribution for the uncertainty estimation as well as to minimize the correlations between the other uncertainty sources.

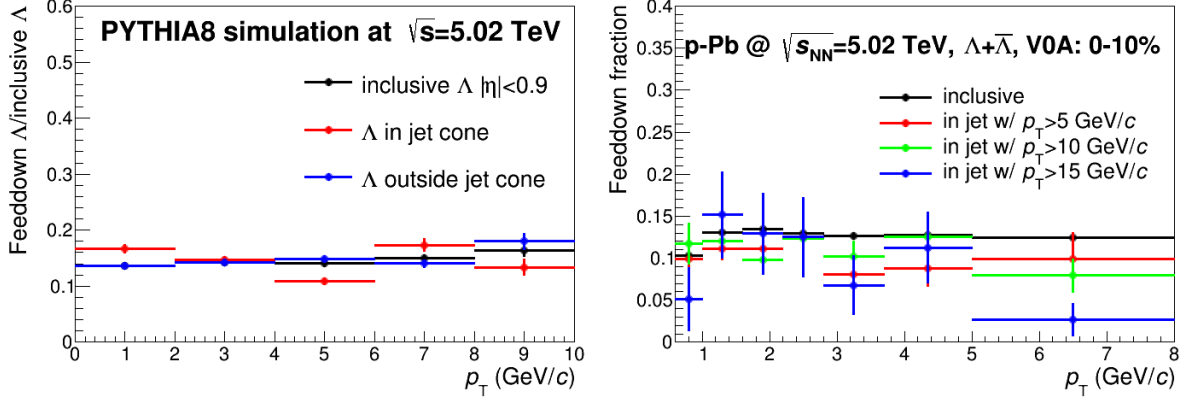


**Fig. 48:** Feeddown fraction of inclusive  $\Lambda$  ( $\bar{\Lambda}$ ) from PYTHIA8 simulations (left) and from the DPMjet simulations (right). The results from PYTHIA8 simulation is obtained at particle level and results from DPMjet simulations is obtained from the detector level.

Since there is no  $\Xi$  data measured in jets, a conservative scenario was applied to estimate the uncertainty on feeddown correction in this analysis.

Figure 48 shows the feeddown fraction of  $V^0$ s in jets and the inclusive  $V^0$ s from the PYTHIA8 (left) and DPMjet simulations (right). The results from PYTHIA8 simulation is obtained at particle level and results from DPMjet simulations is obtained from the detector level. In both PYTHIA and DPMjet, it shows that, the feeddown fraction for both inclusive  $V^0$ s and  $V^0$ s in jets are very similar,  $\sim 10\%$ , and the results are insensitive to the  $p_T$  of  $V^0$ s and jets. While in data, as shown in figure 47, the feeddown fraction of inclusive  $V^0$  shows a weak  $p_T$ -dependence and it is  $\sim 20\%$  at low and intermedia- $p_T$ .

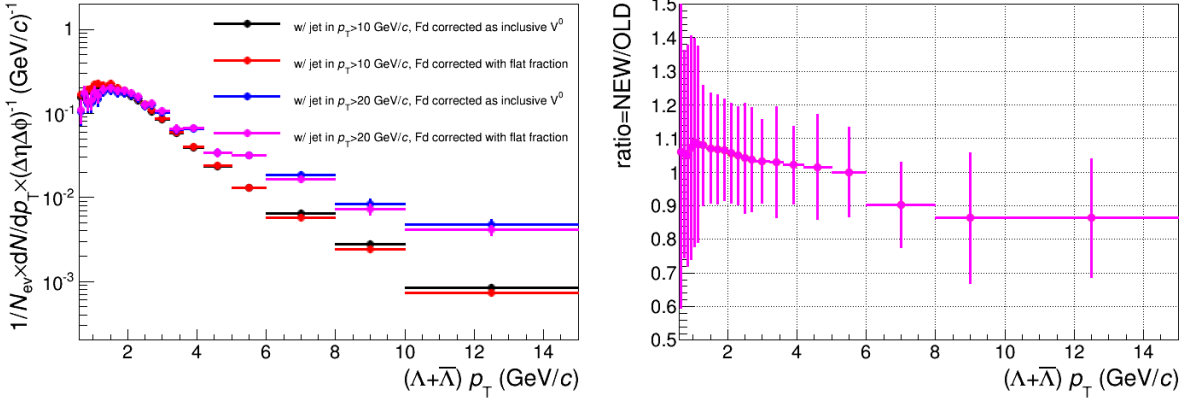


**Fig. 49:** Right: the spectra of JC  $\Lambda+\bar{\Lambda}$  after the feeddown subtraction with different feeddown fraction templates. Left: the ratio between the  $\Lambda+\bar{\Lambda}$  spectra with different feeddown subtraction templates.

According to these studies, we subtract the feeddown component of the  $V^0$ s in jets by using the feeddown fraction of the inclusive  $V^0$ s and a const feeddown fraction as 10%, respectively. The uncertainty on the feeddown subtraction is estimated by using the deviation between the results with these two feeddown templates. Figure 49 shows the feeddown subtracted spectra of  $\Lambda+\bar{\Lambda}$  with different feeddown fraction templates (right) and the ratio between them (left). A maximum 10% deviation is found in the results. In the final results, we used the mean given by these two feeddown fraction templates as the centre value of the spectrum for the  $V^0$ s produced in jets and added and additional 5% uncertainty to the uncertainty on feeddown correction for the inclusive  $V^0$ s.

### 6.2.4 Uncertainty on jet $p_T$

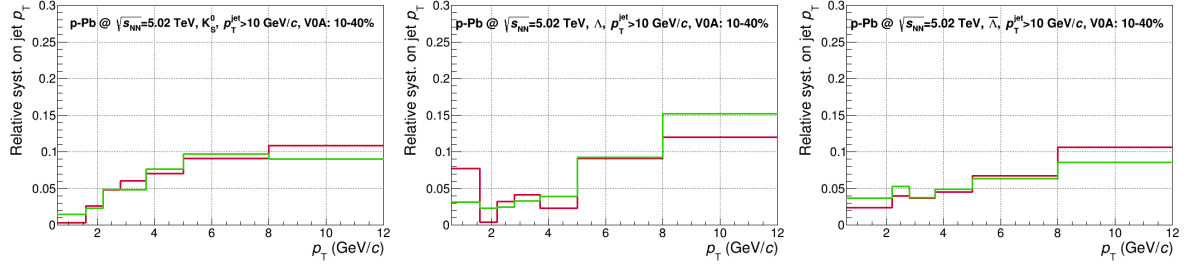


**Fig. 50:** The relative systematic uncertainty on jet  $p_T$  scale. The results are shown in  $10 - 40\%$  event multiplicity bin. The upper and lower uncertainty bands are shown in green and red, respectively.

Indeed, in this analysis, we have to correct both of the reconstructed and acceptance efficiency of  $V^0$ s and the  $p_T$  of the jets. For the jet  $p_T$ , the correction includes the one for the background fluctuations and that for the detector response. In the analysis of the inclusive jet spectra, this correction is applied via an unfolding approach [13]. By considering the  $V^0$  productions inside the jets, the  $p_T$  of  $V^0$ s is correlated with the jet  $p_T$ . And a 2-dimension has to be applied in this analysis. We tried this 2D in our earlier analysis [14], but it is hard to build a stable result due to the less of the statistics.

Alternatively, a bin-by-bin approach has been proposed to correct spectra of particles produced in jets [15]. With this method, the reconstruction and acceptance efficiency of  $V^0$ s, the jet background fluctuations and the detector response of jet  $p_T$  will be corrected synchronously. According to the discussion in section 5.2.2, the efficiency of  $V^0$ s in jets is depend on the jet modified  $V^0 \eta$  distribution. Since the MC can neither reproduce the distribution of  $V^0$ s nor the distribution of jets, the  $V^0$  efficiency calculation should be separated from the bin-by-bin correction. Also, the jet background fluctuations are not well described in MC, even the jet background density in p–Pb collisions is much smaller than that in Pb–Pb collisions.

In this analysis, we calculate the  $V^0$  efficiency via the scaling approach as introduced in section 5.2.2 and treat the effect of the jet background fluctuations and the detector response effect on jet  $p_T$  as the systematic uncertainty.

**Systematic uncertainty on jet background fluctuations** The systematic uncertainty on jet background fluctuations is estimated by varying the jet  $p_T$  threshold in 20%<sup>7</sup> Since the RMS in of the  $\delta p_T$  distribution (as shown in figure 25) is  $\sim 1$  GeV/c, the jet background fluctuations should be included in the band built by varying the jet  $p_T$  in 20% safely. The same as the estimation for the uncertainty on underlying event subtraction, we assume the distribution of the JE  $V^0$ s in the band built by the upper and lower jet  $p_T$  threshold is uniform and give the upper and lower limits of the uncertainty as:

$$\left[ \frac{\text{JE}(p_T^{\text{jet}} > (1 - 20\%)p_T^{\min})}{\sqrt{12}}, \frac{\text{JE}(p_T^{\text{jet}} > (1 + 20\%)p_T^{\min})}{\sqrt{12}} \right]. \quad (34)$$

Due to the production of UE  $V^0$ s is correlated with the jet  $p_T$  threshold, the same approach as defined in eq. (33) is used to estimate the uncertainty in the  $K_S^0$ -to- $\Lambda$  ratio:

$$\left[ \frac{R_{K/\Lambda}^{\text{JE}}(p_T^{\text{jet}} > (1 - 20\%)p_T^{\min})}{\sqrt{12}}, \frac{R_{K/\Lambda}^{\text{JE}}(p_T^{\text{jet}} > (1 + 20\%)p_T^{\min})}{\sqrt{12}} \right]. \quad (35)$$

As an example, the relative uncertainty on jet background fluctuations in the  $V^0$  spectra and that in the  $K_S^0$ -to- $\Lambda$  are shown in figure 50 and figure 51, respectively. The results are shown in  $10 - 40\%$

<sup>7</sup>The uncertainty of  $V^0$ s in jets with  $p_T > 10$  GeV/c is estimated by varying the jet  $p_T$  threshold from 8 to 12 GeV/c. And the uncertainty of  $V^0$ s in jets with  $p_T > 20$  GeV/c is estimated by varying the jet  $p_T$  threshold from 16 to 24 GeV/c.

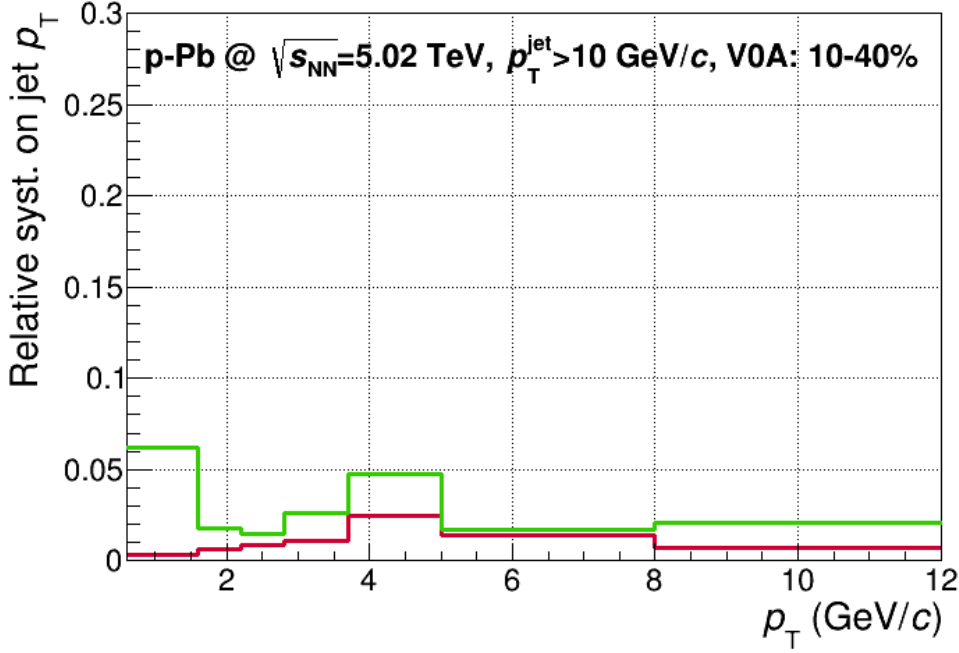


**Fig. 51:** The relative systematic uncertainty on jet  $p_T$  scale in  $K_S^0$ -to- $\Lambda$  ratio. The results are shown in  $10 - 40\%$  event multiplicity bin. The upper and lower uncertainty bands are shown in green and red, respectively.

event multiplicity bin. The upper and lower uncertainty bands are shown in green and red, respectively. The uncertainty in the  $V^0$  spectrum increases with the  $V^0$   $p_T$ . While the uncertainty in the  $K_S^0$ -to- $\Lambda$  is insensitive to the  $p_T$ .

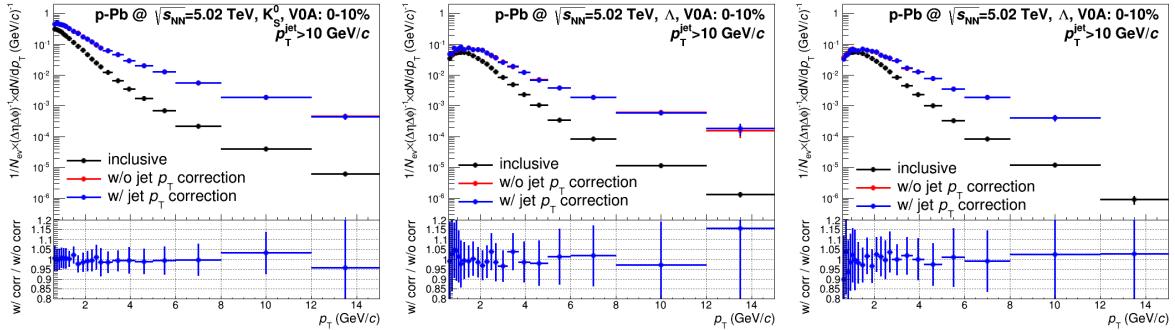


**Fig. 52:** The comparison of the spectrum of  $V^0$ s produced in jets with detector response corrected jet  $p_T$  and that without the detector response correction.

**Uncertainty on detector response** The detector response matrix (as shown in figure 26) describes the effect of the single track efficiency in the reconstructed jet  $p_T$ . The following steps are used to check this effect in the  $V^0$  productions in jets:

1. smear the background subtracted jet  $p_T$  in data with the response matrix and recover it to the particle level;
2. apply the cut on the smeared jet  $p_T$  and redo the analysis to get the  $V^0$  production in jets.

A comparison of the spectrum of  $V^0$ s produced in jets with detector response corrected jet  $p_T$  and that without the detector response correction is shown in figure 52. The difference between the results with

and without the detector response correction is very small. This testing is quite similar as the bin-by-bin correction if only the detector response is considered. In this case, we only use the uncertainty given by varying the jet  $p_T$  threshold within 20% as the uncertainty on jet  $p_T$  scale.

## 7 Results

The final results with different jet  $p_T$  thresholds and event multiplicity estimators are listed in this section:

- figure 53: results in  $p_T^{\text{jet}} > 10 \text{ GeV}/c$  with V0A event multiplicity estimator;
- figure 54: results in  $p_T^{\text{jet}} > 20 \text{ GeV}/c$  with V0A event multiplicity estimator;
- figure 55: results in  $p_T^{\text{jet}} > 10 \text{ GeV}/c$  with ZNA event multiplicity estimator;
- figure 56: results in  $p_T^{\text{jet}} > 20 \text{ GeV}/c$  with ZNA event multiplicity estimator.

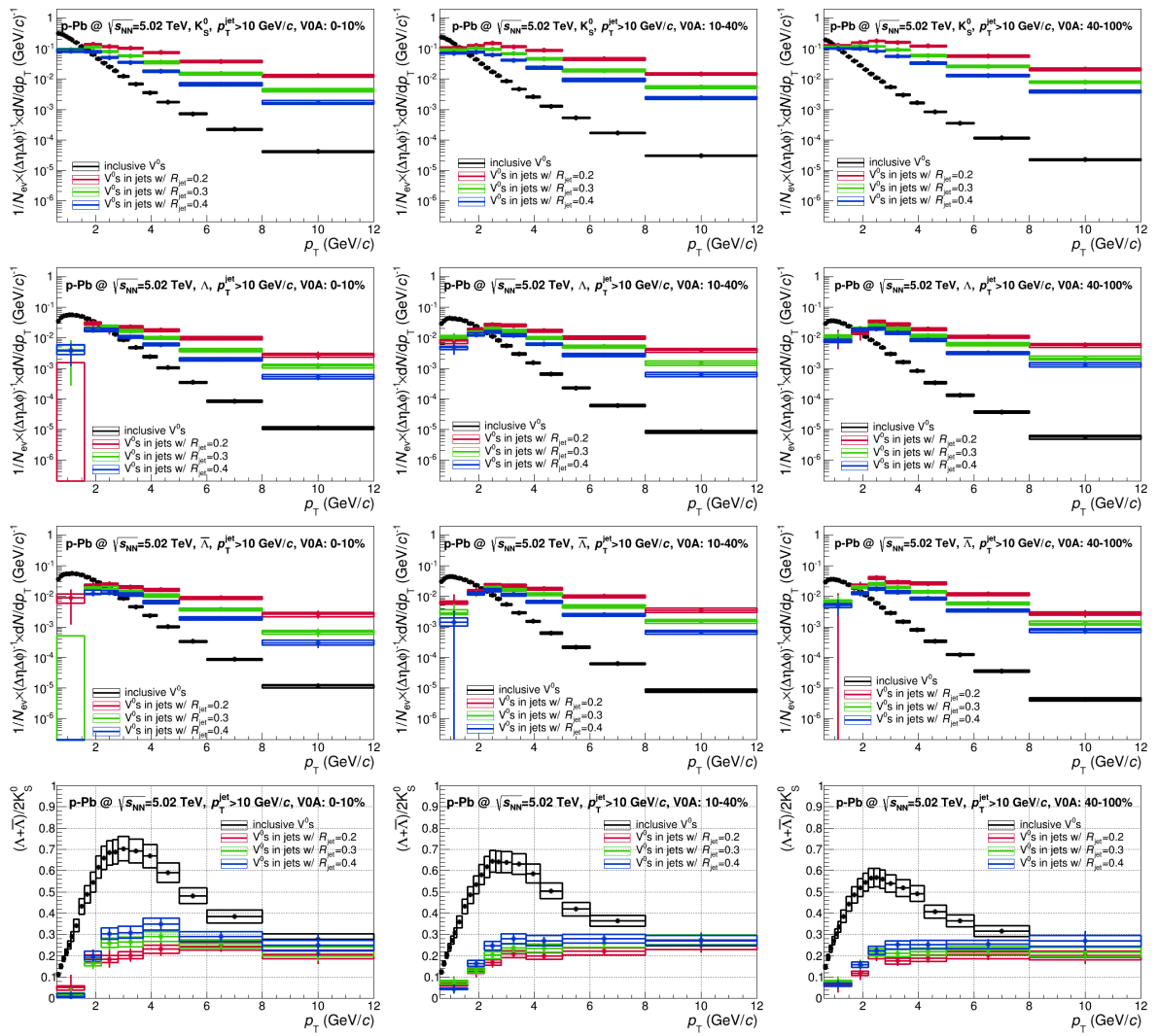


**Fig. 53:** Results in jet  $p_T > 10 \text{ GeV}/c$  with V0A centrality estimator.

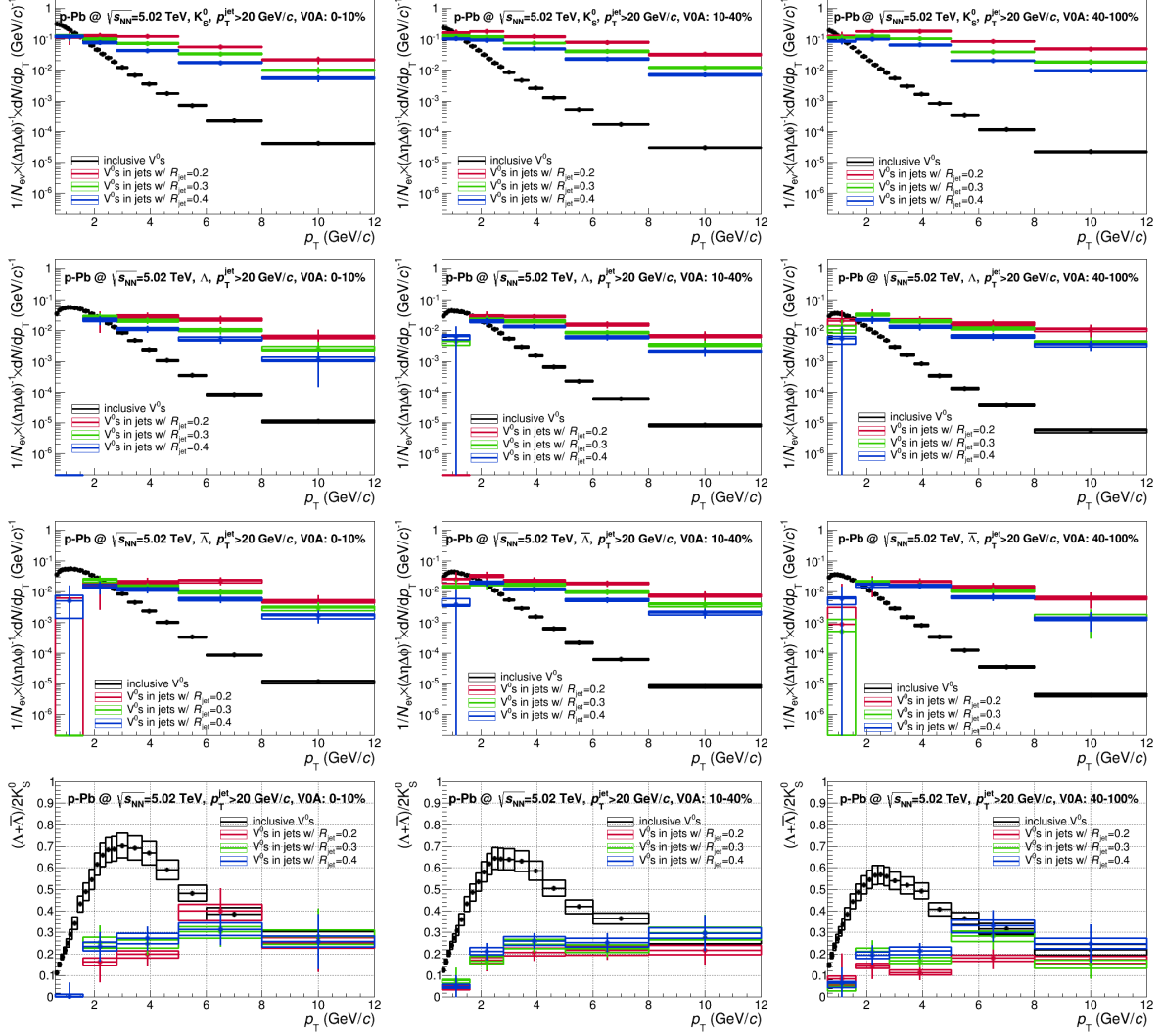


**Fig. 54:** Results in jet  $p_T > 20 \text{ GeV}/c$  with V0A centrality estimator.

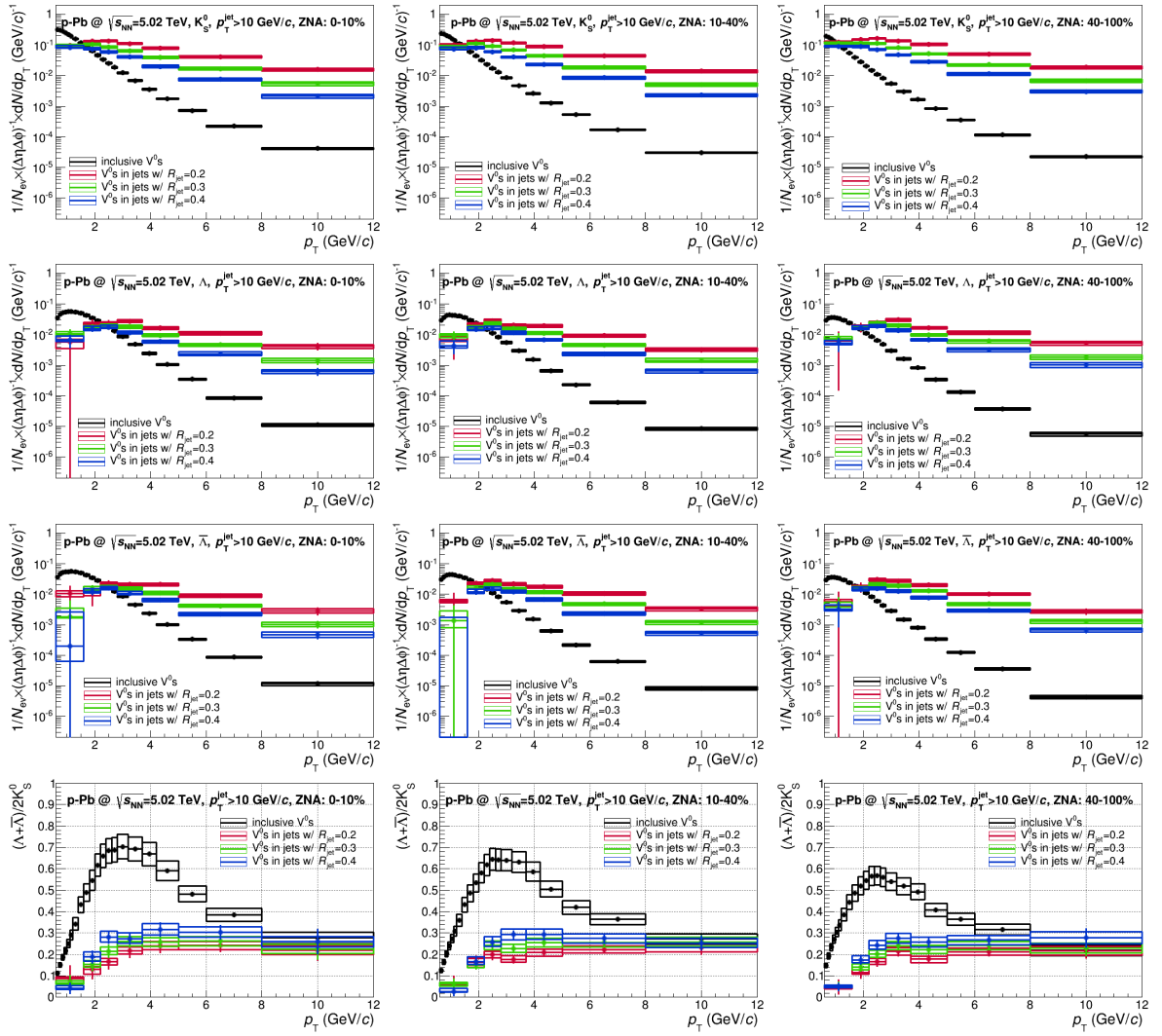


**Fig. 55:** Results in jet  $p_T > 10 \text{ GeV}/c$  with ZNA centrality estimator.

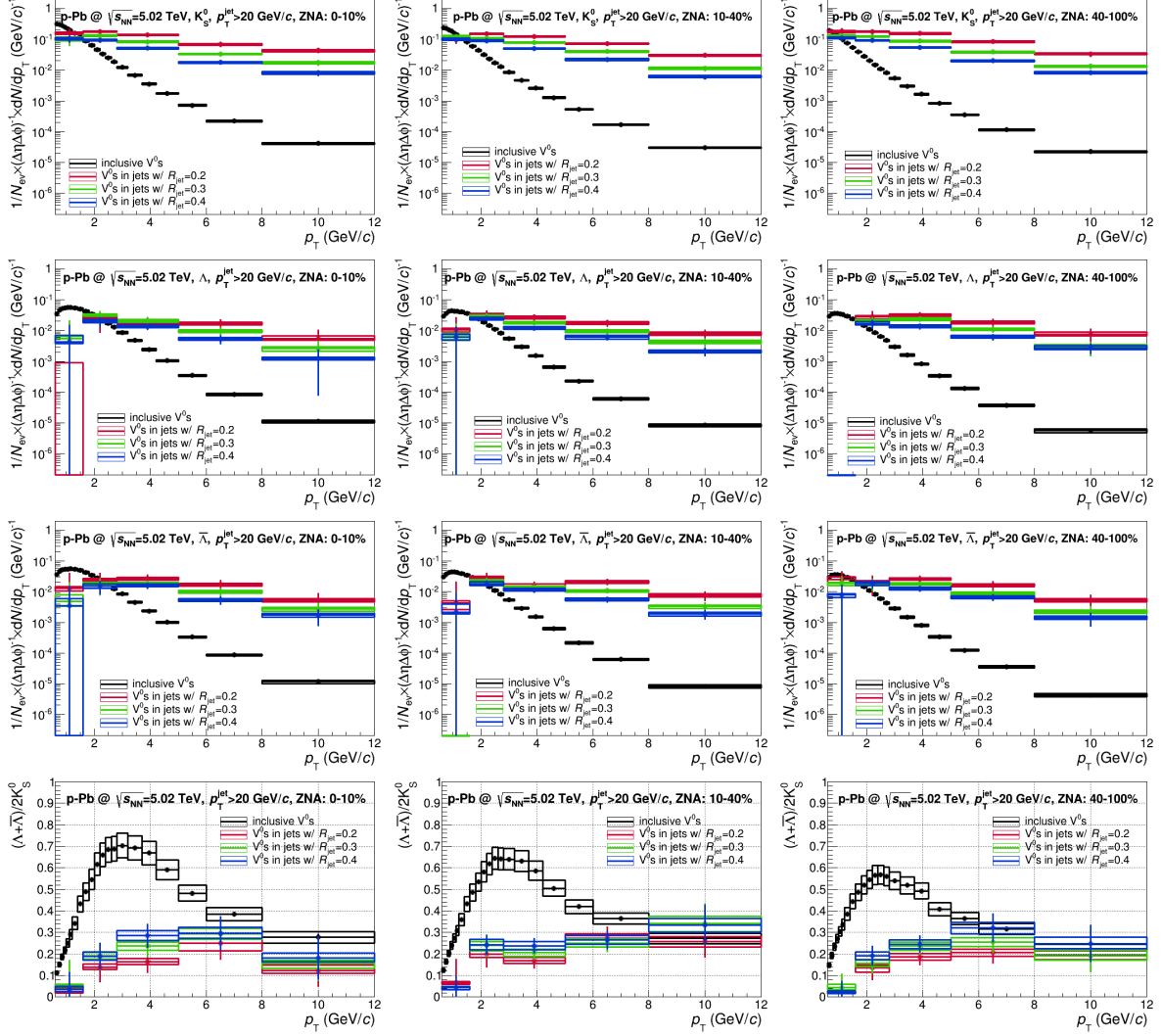


**Fig. 56:** Results in jet  $p_T > 20 \text{ GeV}/c$  with ZNA centrality estimator.

## A V<sup>0</sup> Efficiency Calculation with the Weighting Approach

There is an alternative weighting approach for the JC and OC V<sup>0</sup> efficiency calculation in addition to the scaling approach, which introduced in section 5.2.2, is also studied in this analysis.

The strategy of this approach is:

1. build the  $p_T - \eta$  2D weight according to the ratio of the differential distribution of JC (or OC) V<sup>0</sup> and that of inclusive V<sup>0</sup>s,

$$w_{JC/OC} = \frac{d^2N_{JC/OC}/dp_T d\eta}{d^2N_{inclus}/dp_T d\eta} \quad (A.1)$$

as an example shown in figure A.1;

2. use  $w_{JC/OC}$  as a weight in the calculation of the V<sup>0</sup> efficiency,

$$\epsilon_{JC/OC} = \frac{\sum_\eta w_{JC/OC}(p_T, \eta) \times N_{V^0}^{reco}}{\sum_\eta w_{JC/OC}(p_T, \eta) \times N_{V^0}^{kine}}. \quad (A.2)$$

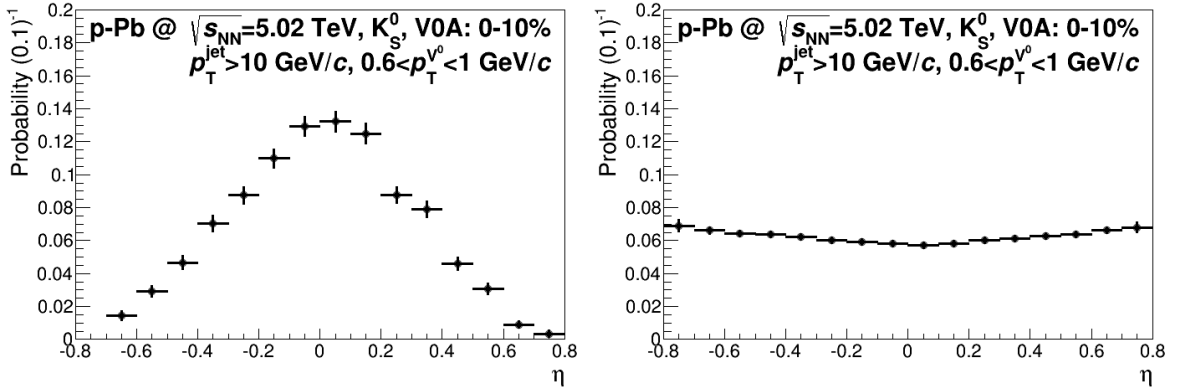


**Fig. A.1:** The  $w_{JC/OC}(p_T, \eta)$  distribution of  $K_S^0$  defined in eq. (??) in  $0.6 < p_T < 1 \text{ GeV}/c$ .

The efficiency of JC and OC (with  $\Delta R > 0.6$ ) V<sup>0</sup>s in  $p_T^{\text{jet}} > 10 \text{ GeV}/c$  and  $p_T^{\text{jet}} > 20 \text{ GeV}/c$  in three event multiplicity bins are shown in figure A.2 to figure A.4. The results are compared to the inclusive V<sup>0</sup>s. The efficiency of  $K_S^0$  ( $\Lambda$ ) in jets is  $\sim 10 - 30\%$  ( $\sim 10 - 20\%$ ) larger than that of the inclusive V<sup>0</sup>s. The efficiency of OC V<sup>0</sup>s is almost the same as that of the inclusive V<sup>0</sup>s.

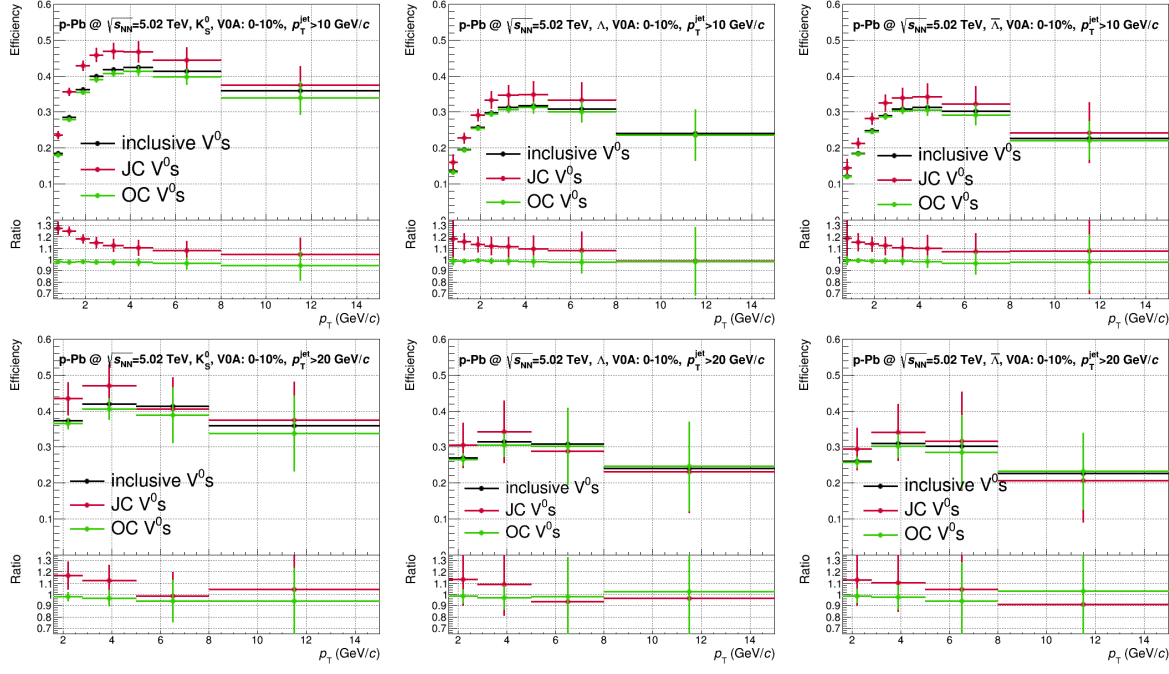


**Fig. A.2:** Efficiency of JC and OC V<sup>0</sup>s in  $p_T^{\text{jet}} > 10 \text{ GeV}/c$  (upper) and  $p_T^{\text{jet}} > 20 \text{ GeV}/c$  (lower) in 0 – 10%. Results are compared to the inclusive V<sup>0</sup>s.

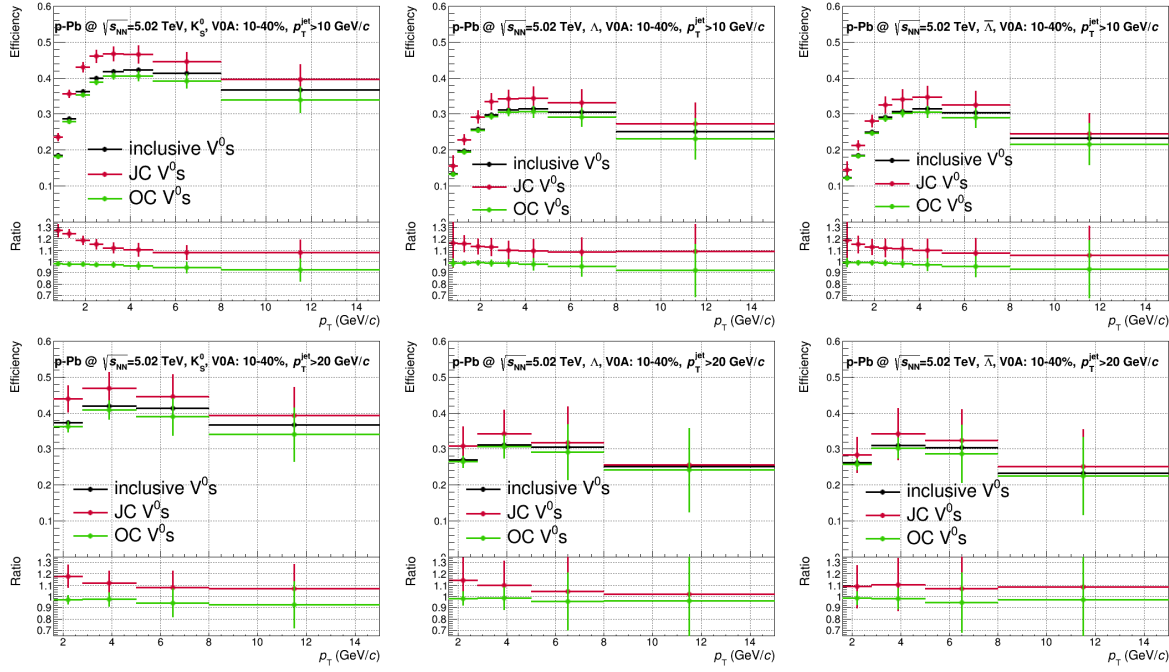


**Fig. A.3:** Efficiency of JC and OC V<sup>0</sup>s in  $p_T^{\text{jet}} > 10 \text{ GeV}/c$  (upper) and  $p_T^{\text{jet}} > 20 \text{ GeV}/c$  (lower) in 10 – 40%. Results are compared to the inclusive V<sup>0</sup>s.

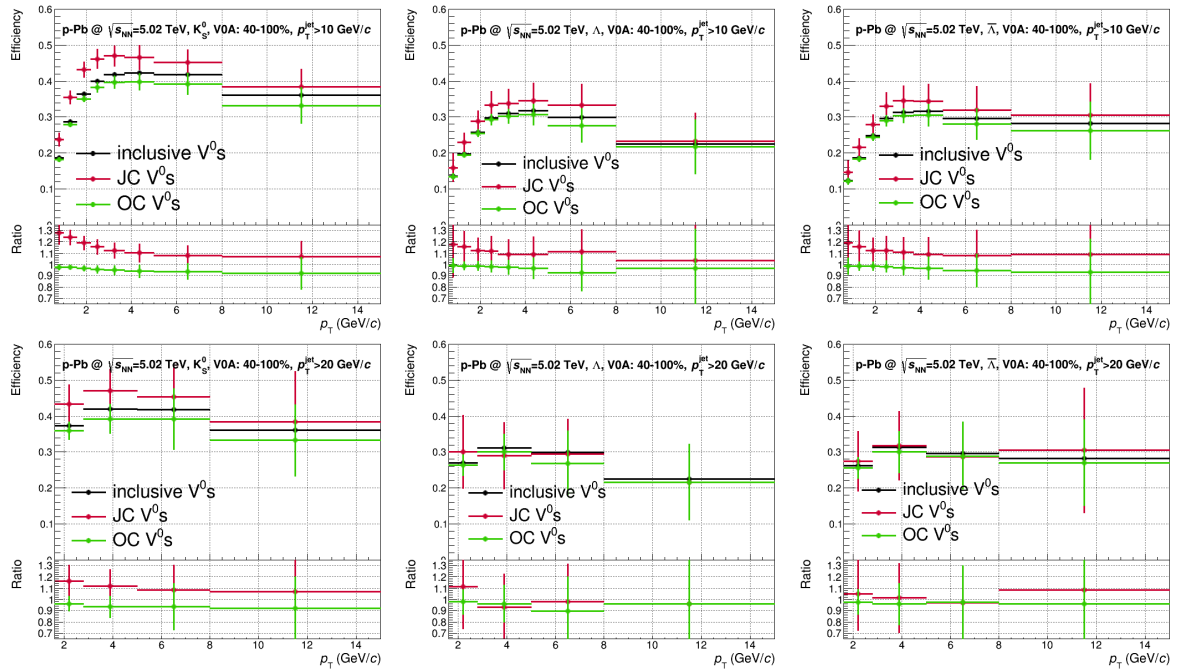


**Fig. A.4:** Efficiency of JC and OC V<sup>0</sup>s in  $p_T^{\text{jet}} > 10 \text{ GeV}/c$  (upper) and  $p_T^{\text{jet}} > 20 \text{ GeV}/c$  (lower) in 40 – 100%. Results are compared to the inclusive V<sup>0</sup>s.

## B Binomial Errors

In general, efficiency is:

$$\varepsilon = r/g, \quad (\text{B.1})$$

where,  $r$  is number of reconstructed particles and  $g$  is number of generated particles. Define:

$$d = g - r, \quad (\text{B.2})$$

eq. (B.1) becomes:

$$\varepsilon = r/(r+d). \quad (\text{B.3})$$

Since  $r$  and  $d$  are the independent variables, the uncertainty of  $\varepsilon$  is given by:

$$\sigma_\varepsilon^2 = \left(\frac{\partial \varepsilon}{\partial r} \sigma_r\right)^2 + \left(\frac{\partial \varepsilon}{\partial d} \sigma_d\right)^2 = \varepsilon(1-\varepsilon)/g, \quad (\text{B.4})$$

where,  $\sigma_r^2 = r$ ,  $\sigma_d^2 = d$ . Eq. (B.4) gives the binomial error for efficiency and it also concludes the statistic uncertainty calculation for the formulae which have the same format as eq. (B.1).

By considering the branching ratio ( $r_b$ ) in the efficiency, the parameter  $d$  in eq. (B.2) has to be redefined as:

$$d = b \cdot g - r, \quad (\text{B.5})$$

then, the binomial error of  $\varepsilon$  becomes:

$$\sigma_\varepsilon^2 = \frac{r_b - \varepsilon}{r_b \cdot g} \varepsilon. \quad (\text{B.6})$$

## References

- [1] D. D. Chinellato. K<sub>S</sub><sup>0</sup>, Λ and  $\bar{\Lambda}$  Spectra in pp collisions at  $\sqrt{s} = 7$  TeV. ALICE-ANA-2012-051, Oct. 2012.
- [2] J. Anielski, D. D. Chinellato, M. Floris, A. Kalweit, and R. Preghenella. Analysis of  $\pi^\pm$ , K $^\pm$ , K<sub>S</sub><sup>0</sup> and Λ ( $\bar{\Lambda}$ ) in p–Pb collisions at  $\sqrt{s_{NN}} = 5.02$  TeV. ALICE-ANA-2013-702, Jun. 2013.
- [3] Betty Bezverkhny Abelev et al. Multiplicity Dependence of Pion, Kaon, Proton and Lambda Production in p–Pb Collisions at  $\sqrt{s_{NN}} = 5.02$  TeV. *Phys. Lett.*, B728:25–38, 2014.
- [4] R. Haake. Minimum Bias Charged Jets in p–Pb Collisions at  $\sqrt{s_{NN}} = 5.023$  TeV. ALICE-ANA-2014-933, March 2014.
- [5] Matteo Cacciari and Gavin P. Salam. Pileup subtraction using jet areas. *Phys. Lett.*, B659:119–126, 2008.
- [6] Matteo Cacciari, Gavin P. Salam, and Gregory Soyez. The Catchment Area of Jets. *JHEP*, 0804:005, 2008.
- [7] Serguei Chatrchyan et al. Measurement of the underlying event activity in pp collisions at  $\sqrt{s} = 0.9$  and 7 TeV with the novel jet-area/median approach. *JHEP*, 1208:130, 2012.
- [8] Betty Abelev et al. Measurement of Event Background Fluctuations for Charged Particle Jet Reconstruction in Pb–Pb collisions at  $\sqrt{s_{NN}} = 2.76$  TeV. *JHEP*, 1203:053, 2012.
- [9] A. Zimmermann. Estimation of K<sub>S</sub><sup>0</sup> reconstruction efficiency in jets – two possible definitions. <https://indico.cern.ch/event/310700/contribution/2/material/slides/0.pdf>, Apr. 2014.
- [10] V. Kučera. Update on V<sup>0</sup>s in charged Pb–Pb jets <https://indico.cern.ch/event/310177/contribution/3/material/slides/2.pdf>, March 2014.
- [11] A. Zimmermann and V. Kučera. Production of K<sub>S</sub><sup>0</sup>, Λ and  $\bar{\Lambda}$  in charged jets in Pb–Pb collisions at  $\sqrt{s_{NN}} = 2.76$  TeV <https://indico.cern.ch/event/311402/session/11/contribution/68/material/slides/0.pdf>, Apr. 2014.
- [12] X. M. Zhang, N. Bastid, and P. Crocht. Measurement of the elliptic flow of muons from heavy-flavour decays at forward rapidity in Pb–Pb collisions at  $\sqrt{s_{NN}} = 2.76$  TeV. ALICE-ANA-2013-921, July 2013.
- [13] M. Verweij, M. van Leeuwen, C. Klein-Bösing, and M. Zimmermann. Measurement of jet spectra with charged particles in Pb–Pb collisions at  $\sqrt{s_{NN}} = 2.76$  TeV with the ALICE detector at the LHC. ALICE-ANA-2012-058, September 2013.
- [14] X. M. Zhang. K<sub>S</sub><sup>0</sup> and Λ ( $\bar{\Lambda}$ ) productions in charged jets <https://indico.cern.ch/event/272865/session/1/contribution/45/material/slides/0.pdf>.
- [15] O. Busch. Charged Particle Momentum Distribution in Jets. ALICE-ANA-2012-067, Apr. 2014.